Probing the photo induced micro actuation properties of optimized Cu doped Co-34at%-Ni-35at%-Al-31at% ferromagnetic shape memory alloys

Abhishek Bagchi [a,*], Vidhyadhar Mishra [b], Suman Sarkar [c], Sandip Bysakh [d], K. Das Gupta [d], T. Maity [d], Amalendu Biswas [e], Susenjit Sarkar [f], P.K. Mukhopadhyay [g], Suman Sarkar [b,c,**]

[a] Department of Electrical Engineering, JLD Engineering and Management College, Baruipur, India
[b] Department of Materials Engineering, Indian Institute of Technology Jammu, Jammu, India
[c] Central Instrumentation Facility, Indian Institute of Technology Jammu, Jammu, India
[d] CSIR-Central Glass and Ceramic Research Institute, Kolkata, India
[e] Department of Mechanical Engineering, Heritage Institute of Technology, Kolkata, India
[f] Department of Mechanical Engineering, Jadavpur University, Kolkata, India
[g] Department of Condensed Matter and Materials Physics, S. N. Bose National Centre for Basic Sciences, Kolkata, India

ARTICLE INFO

ABSTRACT

The strange Photo induced micro actuation (PIMA) properties associated with Cu doped Co-Ni-Al Ferromagnetic Shape Memory Alloys (FSMA) has showed enhancement of mechanical properties in our early studies. This enhancement and optimized PIMA properties have opened a scope of various laser-controlled real engineering applications. In this study, we have explored the microstructural scaling and determined the evolved force due to the laser action in optimized Cu doped Co-Ni-Al alloy system with a detailed insight. This unique PIMA property is rare in literature and actual reason are still not explored. EBSD, TEM, AFM/MFM based techniques were further adopted to understand the role of microstructure in more detail. The evolved magnetic domain patterns for actuating and non-actuating alloys have been analyzed in details. Atomic Force Microscopy was adopted to estimate the constitutive mechanical properties of the thin alloy samples by mechanical spectrometry. This estimation was directly used to predict a general trend in force distribution pattern of the Cu-Co-Ni-Al alloys strips through FEM analysis. The crux of FEM based model and its simulated results can be applied for real time PIMA oriented engineering application and device manufacturing. The detail microstructural exploration and its effect in the PIMA response along with generalized deflection-force model have been presented in the current study.

1. Introduction

The demand of remotely controlled smart actuator materials is increasing day by day for various strategic engineering applications [1–7]. Optically controlled smart actuators in bulk scale system are rare in commercial platform as well as in literature. Ferromagnetic Shape Memory Alloys (FSMAs) nowadays are being applied for customized actuation-based applications [8–10]. FSMAs can be treated as a sub group material belongs to the broader class of well-known system called Shape Memory Alloys (SMAs) [11–14]. Shape memory alloys showed its important role in the engineering application for its exotic microstructural features. They show temperature driven reversible Austenite–Martensite (A-M) transformations which capable them to memorize their pre-deformation shape. Along with this memory property, some group of SMAs also demonstrates super elastic effect via stress-induced reversible thermoelastic martensite transformation. This special property has tremendous role in modern days structural and bio engineering application [15,16]. FSMAs demonstrates exotic and lucrative properties for smart based actuator design. In addition to that, FSMAs also has the capacity to response towards the magnetic coupling to the lattice strain, giving rise to shape changes along with the A-M transformations [17]. These materials have a robust and repeatable response to external stimuli like temperature and force like shear. These properties embedded with quick response against temperature, shear

Table 1

Overall measured alloy composition (atom%) of selected melt spun alloys determined by large scan TEM-EDS analysis. Alloys were prepared in room temperature by vacuum melt spinning technique without any post heat treatment process.

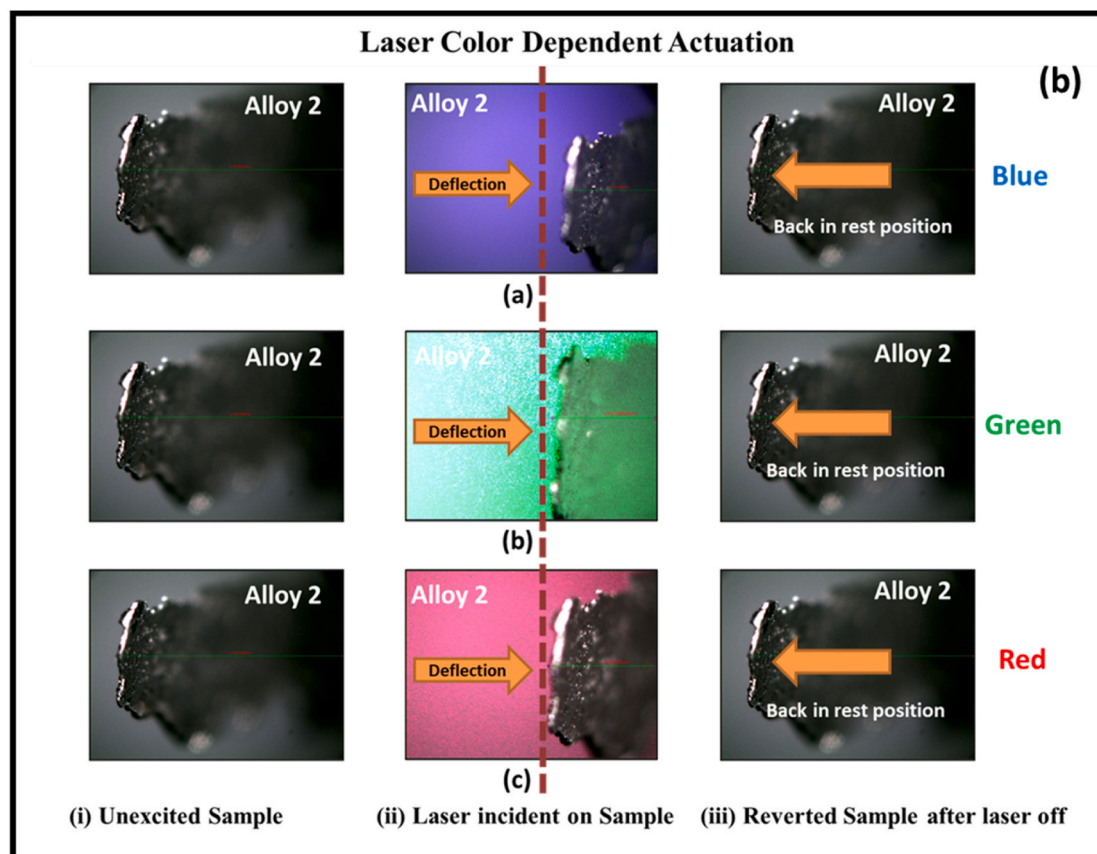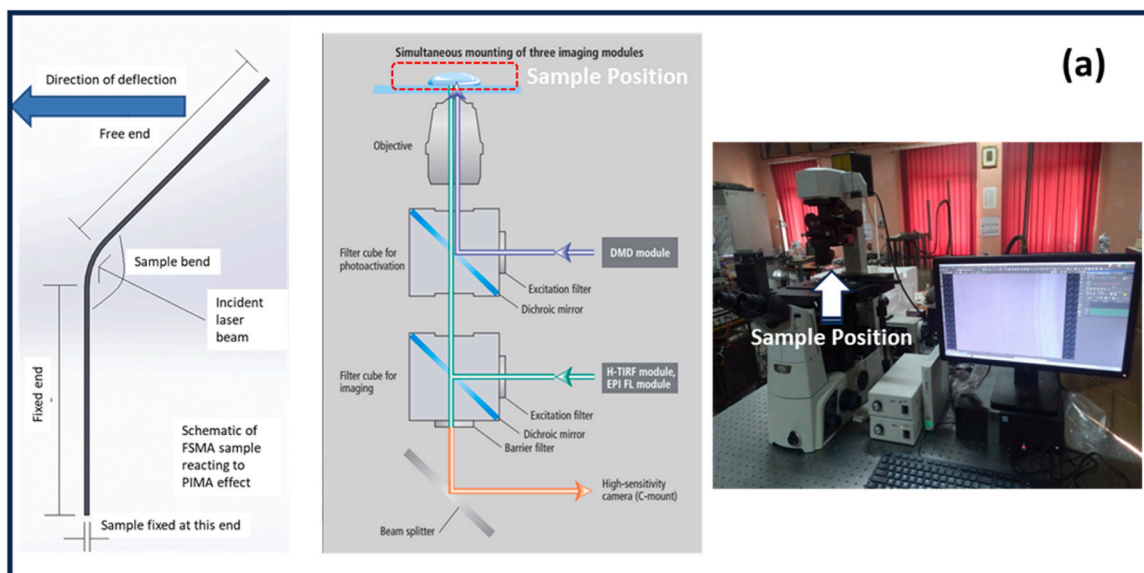| Elements	Co-34 at%-Ni-35 at%-Al-31 at% Alloy 1 (Base Alloy)	Co-32 at%-Cu-2 at%-Ni-35 at%-Al-31 at% Alloy 2 (Used in this study)	Co-24 at%-Cu-10 at%-Ni-35 at%-Al-31 at% Alloy 3	Co-34 at%- at%-Ni-35 at%-Al-21 at%-Cu-10 at% Alloy 4 (Used in this study)
Co	34.1 ± 0.1	31.3 ± 0.4	23.4 ± 0.4	34.2 ± 0.1
Ni	35.3 ± 0.4	34.3 ± 0.5	36.2 ± 0.5	35.3 ± 0.3
Al	30.6 ± 0.3	32.6 ± 0.7	31.0 ± 0.3	20.2 ± 0.3
Cu	—	1.8 ± 0.2	9.4 ± 0.5	10.3 ± 0.4

Fig. 1. (a) Schematic representation of the optical experiment adopted in the current studies. (b) Real time experimental deflection snap shot of the Alloy 2 sample during laser imposition of varied wavelength[24].

Table 2
Experimental value of deflection of the free end of the Alloy 2 strip due to the imposition of Laser Beam of various wattages and colours[22].

Laser Power (mW)	Displacement (mm) (Red – 655 nm)	Displacement (mm) (Green – 532 nm)	Displacement (mm) (Blue – 450 nm)
0	0	0	0
5	0.06	0.068	0.078
10	0.124	0.14	0.16
15	0.19	0.216	0.234
20	0.256	0.292	0.326
25	0.322	0.368	0.408
30	0.382	0.446	0.492
35	0.448	0.524	0.57
40	0.514	0.6	0.646
45	0.58	0.678	0.732
50	0.646	0.754	0.824
55	0.706	0.83	0.912
60	0.768	0.906	0.988
65	0.832	0.978	1.066
70	0.894	1.038	1.138
75	0.958	1.102	1.21
80	1.02	1.174	1.292
85	1.086	1.24	1.374
90	1.144	1.314	1.456
95	1.206	1.388	1.534

force and applied magnetic field have made them suitable candidate for successfully use as sensors and actuators [18–20].

Apart from mechanical and magnetic response, some class of Co-Ni-Al based FSMA system also displays a very strange response against visible light spectrum [21–26]. This property can be termed as Photo Induced Micro Actuation (PIMA) effect [21]. These FSMAs strips showcase deflections when they are stimulated by a focused laser beam. This unexpected and strange property is still not explored in literature and absent in any other materials system till date. This actuation or deflection is also very sensitive function of colour of the light as well as the power of the deployed laser beam. This property was first observed by the P. K. Mukhopadhyay et al. [21]. This optically induced exotic actuation property made this class of alloy potential candidate for remotely controlled device application in various field like medical, electronics and strategic sector [21–26].

Successive works were also carried out towards this direction in the Co-Ni-Al system to probe the real cause of this PIMA effect in connection with the evolved microstructure. The role of other important inherent as well as environment parameter like microstructure, oxidation, temperature etc on this actuation was also studied to make this system engineering suitable [25]. There exists a common trade-off between the mechanical strength and PIMA properties for this system. To make this system viable in real engineering application a detailed work on alloying of copper in the Co-Ni-Al system and simultaneous enhancement of mechanical and optimized PIMA properties have been studied recently [22]. Our subsequent investigation revealed that substitution of cobalt with copper can lead to the enhancement of mechanical strength with some loss of PIMA properties [22]. We have also noted that replacement of aluminium instead of cobalt by copper would cease the PIMA property completely [22]. This was an interesting observation. Finally, the optimized copper addition in order to offer balanced properties and the stability of the microstructure was a concern. Besides this, the optimized alloy also demands a proper analysis of force-deflection response behaviour during engineering application. The present paper reports this effort to address these issues comprehensively.

In this present study, we have taken two directions regarding the Cu-doped Co-Ni-Al system. One is of course to explore the microstructural variants and their role on PIMA properties in order to understand the generalized view of physical cause. The generalized microstructural views can always lead us to harness more similar kind of system with a better and enhanced PIMA properties.

The successful Cu-doped Co-Ni-Al alloy in terms of PIMA and mechanical properties were Alloy 2 and Alloy 3 as explored in the previous study [22]. In our earlier study, an extreme end with 10 atoms% Cu doped Alloy 3's microstructure was analysed where considerable amount of loss in PIMA was observed. In this study, the stability and scaling nature of evolved microstructure of the optimized alloy (Alloy 2) was explored. The composition of all these alloys named as Alloy 1 (the base alloy), Alloy 2 (presently studied alloy), Alloy 3 and Alloy 4 are tabulated in Table 1.

The second approach has been concentrated towards the design of a real actuator assembly capable of showing the PIMA properties. In that quest, we have adopted the Finite Element Model (FEM) based design scheme to understand the estimation of force inserted by laser light on the Cu-Co-Ni-Al FSMA strips. We have tried to simulate the force-deflection pattern of the alloy system from experimental deflection data [22]. This understanding will give an insight to design a real time engineering device capable of showing remotely controlled actuation. In this way, we have tried to address both microstructural role on PIMA properties and validate the experimental data with the adopted simulation in order to make a photo sensitive actuator device.

Electron Back Scatter Diffraction (EBSD), Transmission Electron Microscopy (TEM), Atomic Force Microscopy (AFM) and Magnetic Force Microscopy (MFM) based techniques were further adopted to understand the role of microstructure in more detail. Atomic Force Microscopy was adopted to estimate the constitutive mechanical properties of the thin alloy samples by mechanical spectrometry. This estimation was directly used to predict a general trend in force-deflection behavior of the Cu-Co-Ni-Al alloys strips. The crux of FEM based model and its simulated results can be applied for real time PIMA oriented engineering application. The detail microstructural exploration and its effect in the PIMA response along with generalized deflection force model have been presented in the current study. A microstructural comparison between three studied alloys (un-doped Alloy 1, Alloy 2, Alloy 3 and Alloy 4) were also included for continuation and completeness.

In a summary note, the present study has been focused towards the exploration of generic nature of the microstructure responsible for this actuation. We have generalized the length scale stability, repeatability, required for the microstructural design in the present study. In this study, we have also looked at whether the surface plasmonic effect is really a necessary vector for actuation through STEM-EELS technique. The present study has looked at the role of magnetic domain of the photo active phases. The substitution or doping effect for property optimization are also established in this present study. We have concentrated our efforts towards the determination of the numerical values of invisible force during laser action. This set of force data can be utilized for real time sensor application. This study will also offer the force-deflection pattern identification in other electromagnetic domain-based actuation (like infra-red based actuation). This force-deflection distribution pattern can be evaluated from the FEM simulation results by extending its model parameter. All the information, holistically explored in the current study are now generalized in nature and can be amalgamated during photo-sensitive based product design.

2. Experimental details

Alloy samples were synthesized by melting the 99.99% pure constituent elements under argon environment using an arc melting unit. These alloy ingots were then subsequently melt-spun in a high vacuum rotating melt spinning unit with wheel speed of 600 rpm to produce the ribbons strips. Copper has replaced the Co and Al with three varying compositions in the base alloy and the detailed nominal and measured compositions along with the nomenclature scheme for current study are shown in Table 1. All the alloys were prepared in room temperature by vacuum melt spinning technique without any post heat treatment process.

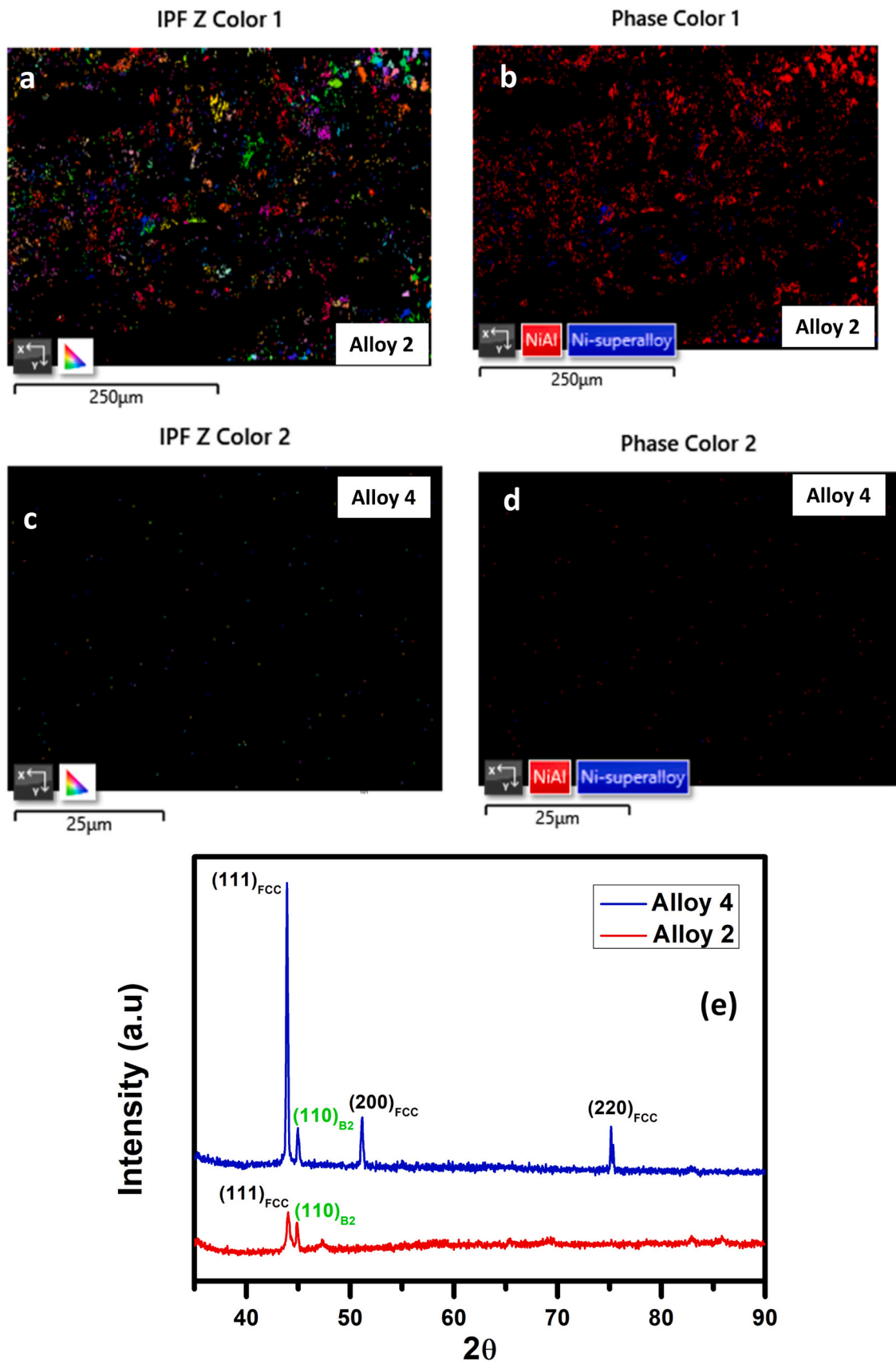**Alloy 1** (Table 1) is the base alloy without any alloying whereas,

Fig. 2. (a) and (b) A corresponding IPF and Phase Colour Map for Alloy 2. (c) and (d) A corresponding IPF and Phase Colour Map for Alloy 4. (e) Comparative XRD plot between Alloy 2 and Alloy 4[22,25].
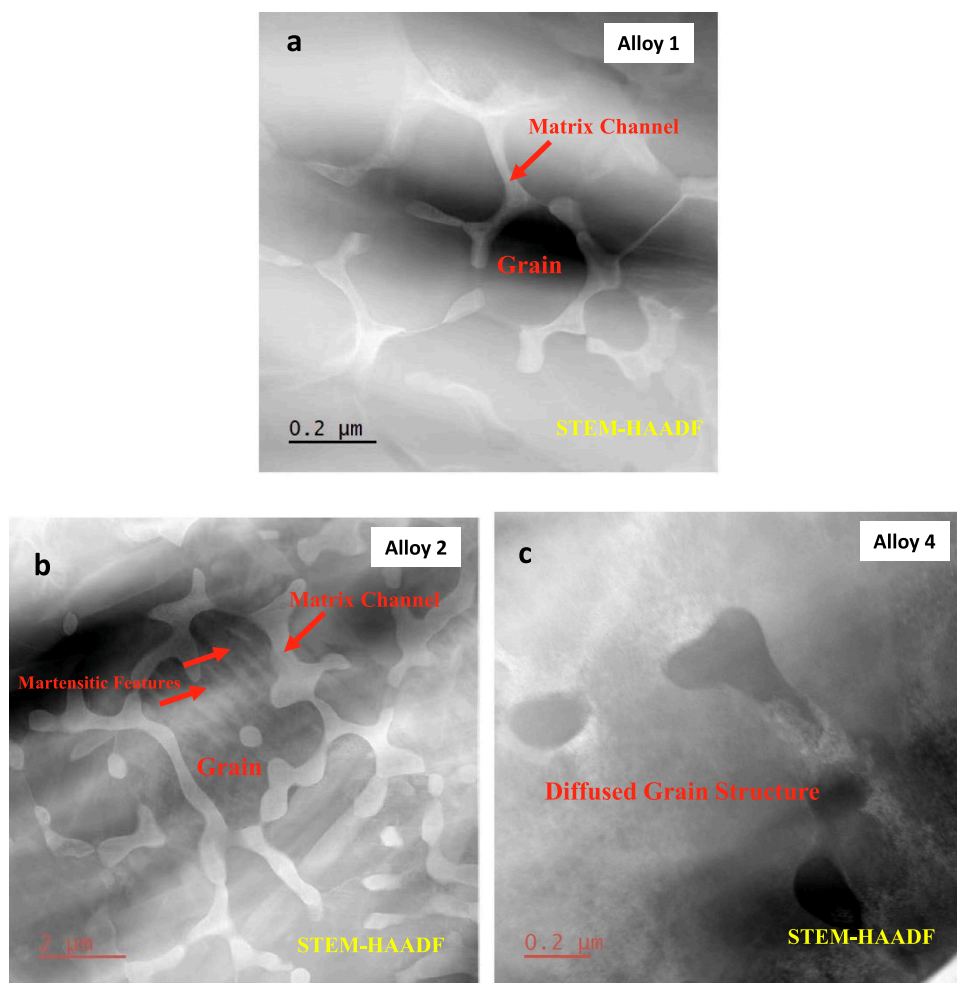
Fig. 3. (a) and (b) and (c) Represent the STEM-HAADF micrograph of three studied alloys. Figure (b) has been taken in higher magnification to resolve the martensitic features inside the microstructure of Alloy 2.

Alloy 2 (Table 1) (Co is replaced by Cu-2 at%) is the optimized and presently studied alloy. The limiting copper doped **Alloy 3** (Table 1) (Co is replaced by Cu-10 at%) was studied earlier with details and results extracted from the study, lead us to design **Alloy 2** as a real engineering actuator for optimized PIMA and mechanical properties. **Alloy 4** (Table 1) (Al is replaced by Cu-10 at%) does not showcase any actuation and studied thoroughly as for comparison from the evolved microstructural viewpoints.

The detailed structural and chemical analysis of the melt spun alloy samples was carried out in the JEOL make JEM-ARM200F model transmission electron microscope (TEM), by using the scanning TEM High-angle Annular Dark-Field (STEM-HAADF) imaging and spectrum-image elemental-mapping technique involving the Energy Dispersive X-ray Spectrometer (EDS). Attached Electron Energy Loss Spectroscopy (EELS) spectrometer with the TEM was used for collecting the energy loss related information arising from the inelastic type of scattering of electron with the sample. The TEM specimens were prepared by ion milling the samples using argon ion beam inside a Gatan precision ion polishing system (PIPS) operating at an accelerating voltage of 5 kV and 4° incidence angles on both sides of the melt-spun foils to reach the desired specimen thickness. The overall composition analysis and EBSD (Electron Backscatter Diffraction) study was performed in a JEOL make FE-SEM (Field Emission-Scanning Electron Microscope) (JSM 7900 F model). The EBSD technique collects locally acquired Kikuchi patterns in order to retrieve the crystalline phase information of the pattern-forming sample volume [33]. It displays the changes of a property with changing crystal orientation. The inverse pole figure (IPF) colour

code scheme is efficient analytical technique to detect phase orientation information. A systematic IPF colour maps with detection of probable phases was collected from the crystallographic data base associated with the SEM instrument software.

The Mechanical spectrometry and surface topography of the thin alloy strip were carried out in an AFM instrument (Veeco having model no. di INNOVA). The AFM was employed to study the mechanical properties of the samples [27–30]. The Silicon Nitride probe was used to carry out the contact mode point spectroscopy studies of the samples. The cantilever spring constant (k) of the used probe was 0.58 N/m. The shape of the tip of the probe was Square Pyramidal having a tip half angle (α) of 35°. The MFM was carried out in an OXFORD make instrument (Cypher Universal Enclosure). The tip used in this study is made of silicon with a CoCr alloy coated feature. The tip was magnetized with a hard magnet in the perpendicular direction of the prob tip surface and tapping mode was used during scanning of sample surface. The lift height of the tip was 50 nm. The cantilever resonance frequency was preset at 75 kHz with a spring constant of 2.8 k(N/m). A 2-dimensional ferromagnetic domain maps were generated from localized interaction of stray magnetic field of sample and the MFM probe tip [58–60]. The phase shift due to the magnetic interaction produced in the oscillatory MFM cantilever was processed for generation of the magnetic domain maps.

As there is no device to measure tiny force experienced by the alloy sample during laser incidence, help of numerical simulation has been taken for this force measurement following an optimization method named Response Surface Methodology [26, 61–62]. To execute this
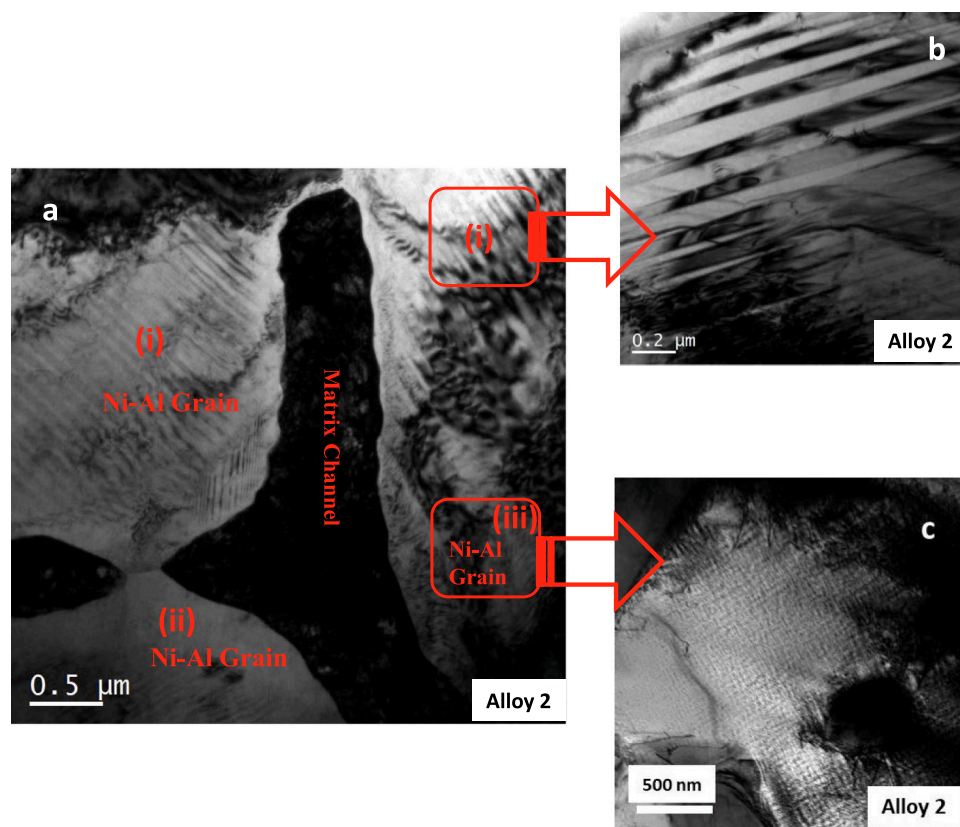
Fig. 4. (a) A bright field image of the Alloy 2 showing the presence of graded component inside the microstructure. (b) Distribution of martensitic plates. (c) Evolution of tweed type compositionally fluctuating spinodal microstructure.

numerical simulation for the determination of tiny forces causing given deflections, a FEM software, named "ANSYS 2020 R1", has been used along with its Optimization module. A 3D model of the FSMA alloy strip has been developed in a CAD software named SolidWorks 2022 and then imported in ANSYS for detailed simulation and computation of the evolved forces [63].

Optical experiments were conducted on samples of similar size and shape as used in the earlier experiments [22–25]. A Nikon made Eclipse Ti-U model dual deck inverted research microscope along with a SHO-DENSHA High Resolution 2-Megapixel USB Microscope were used to observe the micro-actuation of the sample using the associated software. One of the decks of the Ti-U model microscope was applied to focus the falling laser beam spot onto the sample through an attached objective lens. A half mirror arrangement was used to pass the laser beam and capture the deflection in the camera attached with the microscope. A schematic of the microscope structure and operation along with the conducted optical experiment are shown in Fig. 1(a). The microscope schematic has been taken from "Nikon Eclipse Ti-U inverted microscope" user manual [26]. The real time video snaps of induced deflection due to the falling of laser beam of varied wavelength on the sample are shown in Fig. 1(b) as an image series for the studied alloy [24]. Fig. 1(b) shows the variation in the deflection for each of the three laser diodes used for this experiment. The nominal optical power output of 95 mW with a wavelength of 655 nm for the red, 450 nm for the blue and 532 nm for the green laser were used respectively [22]. It can be also noted from figure1(b) that the highest deflection can be achieved from the blue color laser. The numerical values of the photo induced actuation are also tabulated in Table 2 [22]. All optical experiments were carried out at a controlled ambient temperature of 25 °C and at a constant relative humidity of 45% as reported earlier [21–25]. The experimental photo induced actuation data for all the studied alloy samples are available in the earlier literature and also has been presented in Table 2 [22,22–25].

This actuation data for Alloy 2 were directly used in the present FEM model for force calculation.

3. Results and discussions

3.1. EBSD and XRD analysis and phase determination

The present study hints that presence of Ni-Al rich and crystallographically B2 ordered phase can only lead to the observed photo actuation as observed earlier [22–25]. Alloy 2 shows the optimized deflection during laser incidence and expected to have the similar type of phase morphology in the structure [22].

In this current study, we have adopted EBSD based phase analysis technique to probe the bulk surface level information regarding the presence of PIMA active Ni-Al ordered phase in the synthesized samples [31–33]. A representative IPF X, Y and Z colour map and corresponding phase colour map have been collected and IPF Z is presented in Fig. 2 for the two alloy sets namely Alloy 2 and Alloy 4. A guiding unit stereogram is also included for the maps. Fig. 2(a) and (b) clearly depicts that probable PIMA active B2 ordered Ni-Al phase which was captured through the EBSD data base is only present for the case of alloy 2. Whereas one can notice that no traces of Ni-Al phase was detected for PIMA vanishing alloy 4 (Fig. 2(c) and (d)). This information establishes the fact that presence of Ni-Al phase as a microstructural component has the direct effect on enabling photo induced actuation. For the sake of continuation and completeness, we have also included a comparative XRD plot from our earlier studies for the two alloys in Fig. 2(e) [22,25]. Fig. 2(e) shows the structural difference between PIMA active Alloy 2 and non-actuating Alloy 4. The $(110)_{B2}$ ordered PIMA active phase can be noticed for both the alloys. A careful observation will disclose that a significant phase evolution with FCC based signature peak has emerged for the case of Alloy 4 (Fig. 2(e)). This comparative XRD based structural
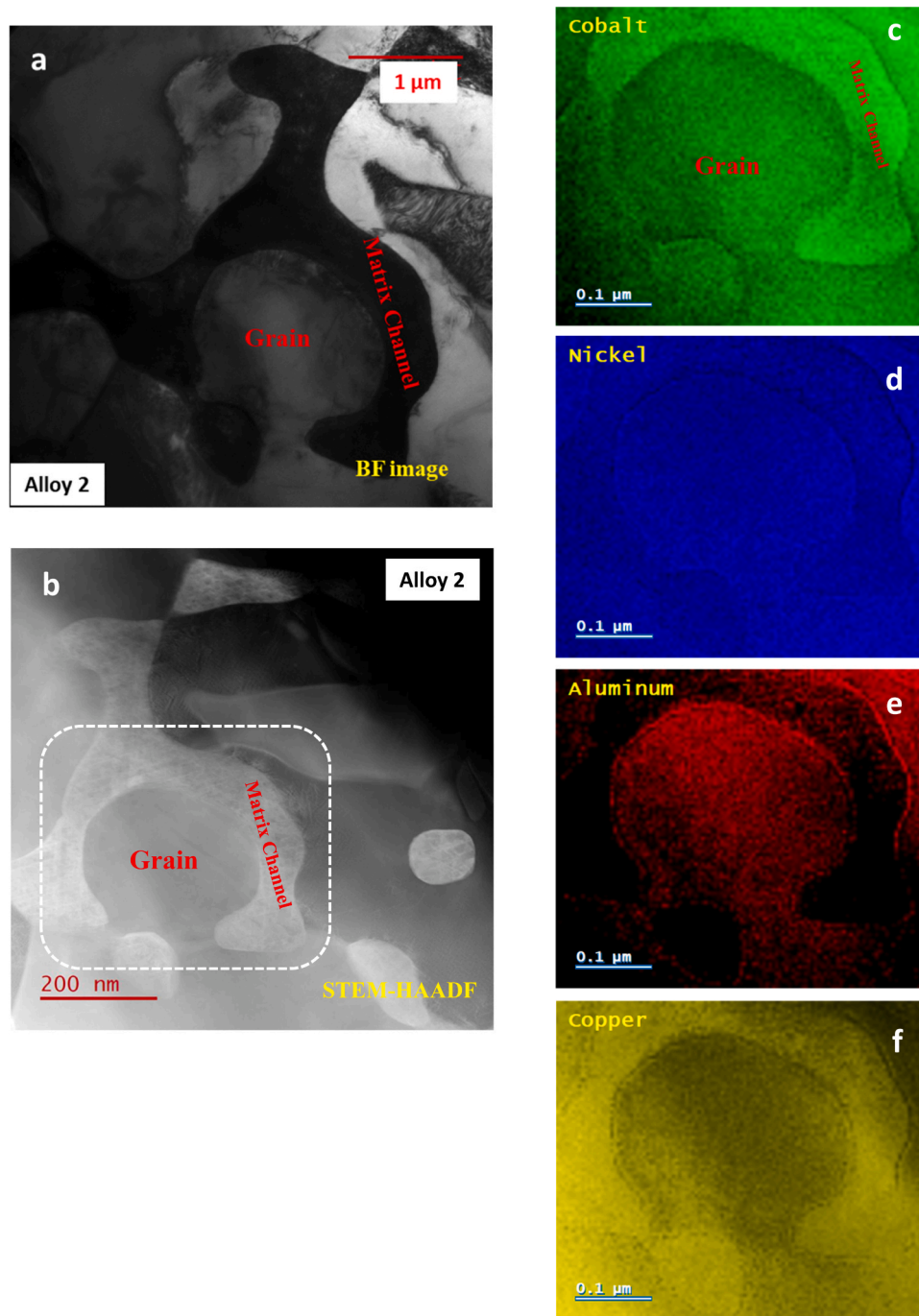
Fig. 5. (a) and (b) A bright field and corresponding STEM-HAADF image of the Alloy 2. (c-f) Spatial Elemental distribution maps derived from EELS high loss spectrum.

study hints towards the microstructural difference between two alloys. We have discussed this microstructural difference in the following section with deep insight (Fig. 11).

3.2. Microstructure evolution

The details of the evolved microstructure were observed through transmission electron microscope. Representative STEM-HAADF based atomic number contrast (Z) micrographs are shown in Fig. 3. Fig. 3 comprehensively present a comparative microstructural difference between three studied alloys (Alloy 1, Alloy 2 and Alloy 4). The detailed diffraction analysis of three studied alloys can be found in our earlier

work [22–25]. We have also included the STEM-HAADF image of undoped Co-Ni-Al alloy (Alloy 1) in this current paper (Fig. 3(a) for the sake of completeness and comparison. Fig. 3(a) shows the atomic number or Z-contrast image of pure Co-Ni-Al alloy (Alloy 1). This microstructure contains two type of distinct features and can be categorized as PIMA active B2 ordered Ni-Al grains which are embedded in the FCC based L1$_2$ ordered matrix channel. The evolved microstructure of the Alloy 2 only differs in terms of the presence of martensitic plates, emanated inside the B2 ordered grain (Fig. 3(b)) (Red arrow marked in the Fig. 3(b)). Fig. 3(c) shows the evolution of diffused grain like structure with no prominent matrix and grains interface for the Alloy 4 sample. This comparison based microstructural information exhibits
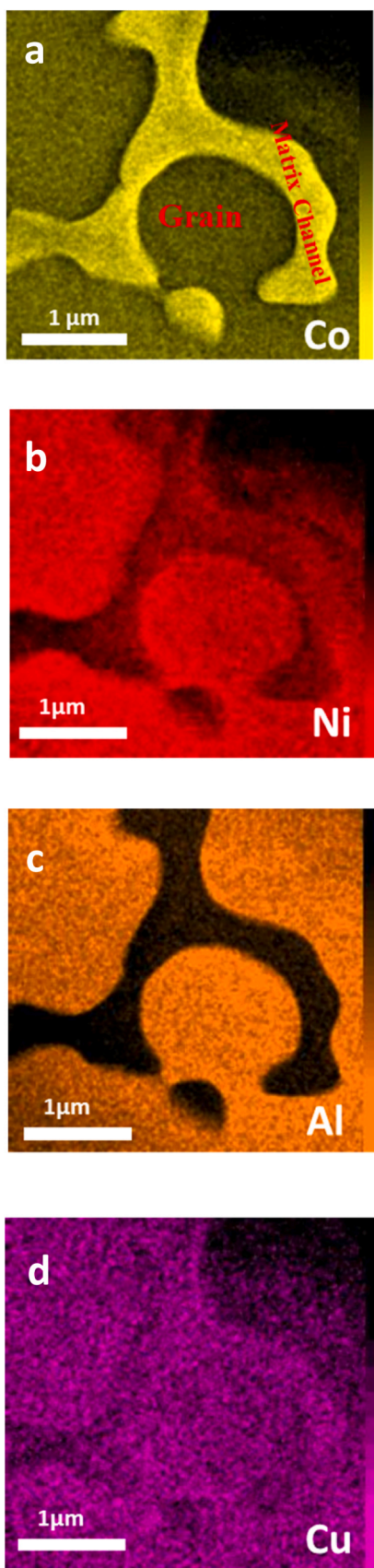
Fig. 6. (a-d) STEM-EDS spatial elemental mapping showing that grains are rich in Ni and Al and the matrix is rich in Co.

that the replacement of cobalt with copper (for Alloy 2) modifies the microstructure. But in this case, the sharp interface between B2 ordered Ni-Al grains and the L1₂ ordered matrix phase are still present like the undoped alloy (Alloy2). On the other hand, the replacement of aluminium with copper (Alloy 4) can significantly alter the microstructure.

In this present study, we have concentrated our focused in extracting the diminutive structural details of the potential Alloy 2 for PIMA related real scale engineering application. The melt spun microstructure of the Alloy 2 shows three distinct types of microstructural components. A representative TEM bright field (BF) image as shown in Fig. 4(a), displays the presence of three prominent microstructural attributes. They can be categorized in the following way.

(i) Some of the Ni-Al B2 ordered grains contain martensitic plates (Fig. 4(a), marked as (i) in red colour and Fig. 4(b)).
(ii) Grains with clean Ni-Al B2 ordered type feature with sharp matrix-grain interfaces are also visible and similar to undoped Alloy 1 (Fig. 4(a), marked as (ii) in red colour).
(iii) Few Ni-Al B2 ordered grains demonstrate tweed type of contrast (Fig. 4(a), marked as (iii) and Fig. 4(c)) [34–36].

This time, we have adopted EELS based spectroscopic technique to extract the finer details of the evolved microstructure of Alloy 2. Spatial elemental distribution maps have been extracted after proper fitting and background manipulation from the core loss region of EELS spectra. A TEM bright field and corresponding STEM-HAADF image from the same location are also shown in Fig. 5(a) and (b) respectively for eye guidance. The EELS extracted maps are shown in Fig. 5(c-f). The spatial elemental distribution maps manifest that the grains are rich in Ni and Al whereas, matrix channels are rich in Co and Cu. A careful observation will also hint that some amount of Co and Cu are partitioned inside the PIMA active Ni-Al grains. A complementary qualitative STEM-EDS spatial elemental distribution maps are also shown in Fig. 6(a-d). These maps also confirm the resemblances of the elemental distribution as derived from the EELS technique. This spectroscopic result confirms that the replacement of cobalt by 2 at% of copper also lead towards the production of scalable microstructure as noticed in the earlier studies (with considerable amount of copper substitution) [22–25].

In this study, we have looked into the evolved tweed type of morphology in a greater detail. A TEM bright field (diffraction contrast) and corresponding STEM-HAADF ('Z' atomic contrast) images taken in a different magnification are shown in Fig. 7(a) and (b) respectively. Fig. 7(b) shows that tweed contrast with fluctuating composition is originated inside the grain for the case of Alloy 2. The density of the tweed type contrast is homogeneous throughout the microstructure. An STEM-EDS based spatial elemental distribution maps are shown in Fig. 8(c-f). The elemental distribution maps qualitatively display the homogeneous presence of participating elements in the tweeded zone of the Ni-Al ordered grain. In these maps, it is also clear that the matrix channel is rich in cobalt and copper, whereas devoid of aluminium and nickel. A guiding white arrow has been marked in each map to display this information (Fig. 8(c-f)). An additive RGB (Red-Green-Blue) composite map derived from the superimposed elemental maps is also shown in Fig. 8(b). This RGB map indicates towards the fluctuating compositional gradient of the participating elements. This homogeneous composition fluctuation in the entire microstructure as seen in Fig. 8, can be linked with the case of incipient spinodal decomposition [37–41]. This type of tweed contrast can be ascribed due to the originated strain field, caused by the relative displacement of the fluctuating atoms in some preferred crystallographic direction [34–36]. This composite elemental distribution RGB map, as seen in Fig. 8(b) indicates the spinodal type atomic fluctuation is the probable cause of tweed domain formation inside the PIMA active B2 ordered Ni-Al grain. Interestingly, it can also be qualitatively noticed that the equal partitioning of copper has been taken place between the matrix and grains in this incipient phase
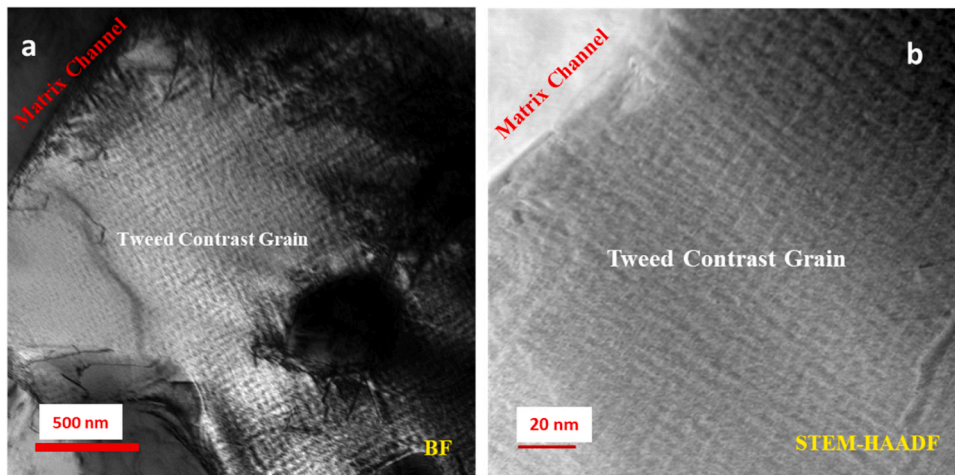
Fig. 7. (a) A bright field image showing the evolution of tweeded type microstructural attributes inside the grain. (b) Corresponding STEM-HAADF image showing the composition fluctuation inside the grain.
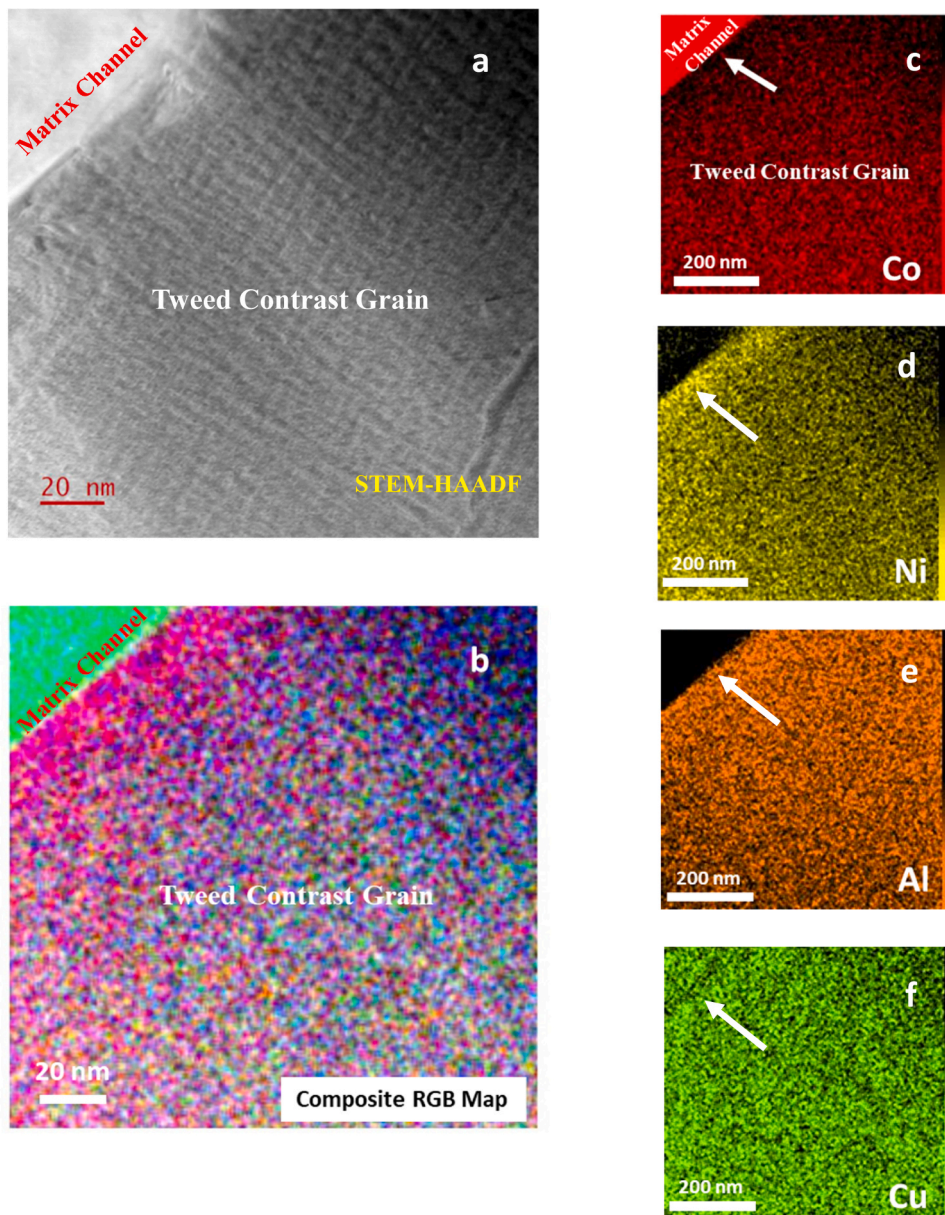

Fig. 8. (a) A representative STEM-HAADF micrograph showing the tweed microstructure with composition fluctuation. (b) A RGB composite map showing the equally partitioned composition fluctuation. (c-f) STEM-EDS spatial elemental mapping showing the composition fluctuation inside the grain.
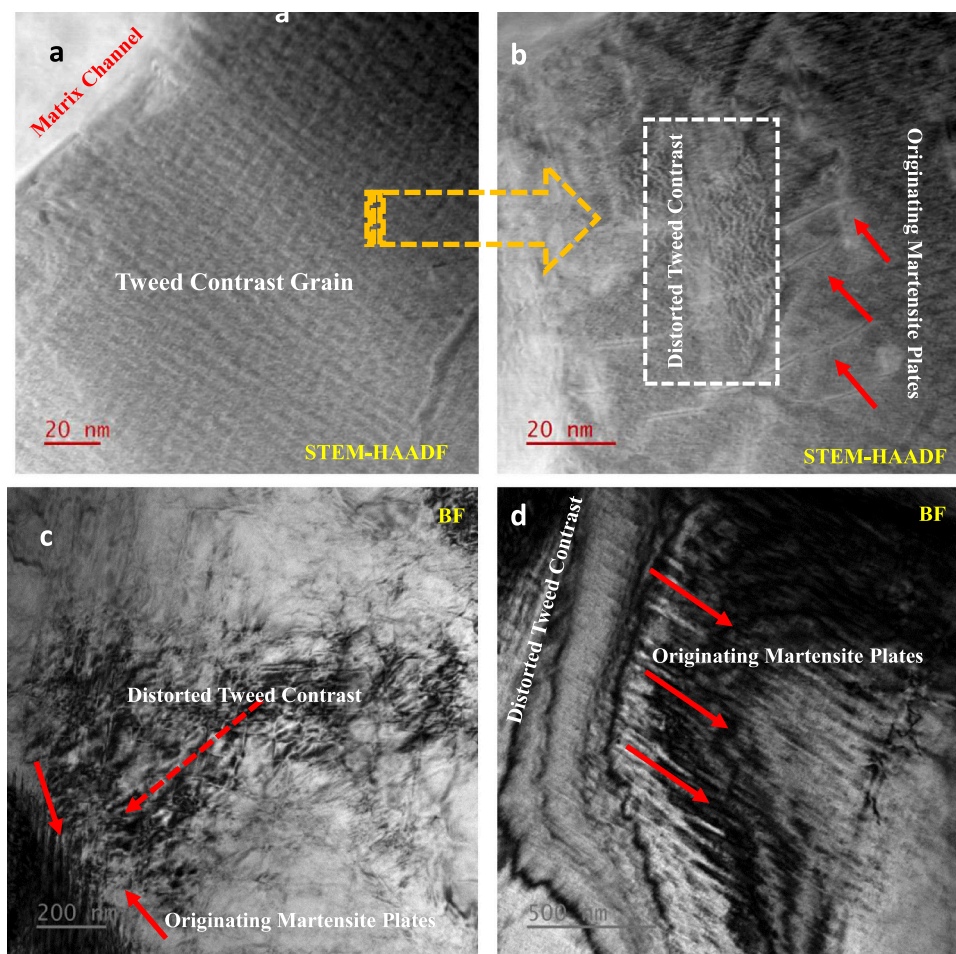
Fig. 9. (a) A STEM-HAADF image showing the tweed contrast inside the grain (b) Transformation of tweed type modulation towards the martensitic plate as a precursor of martensitic nucleation. (c) A snap shot moment of transformation of tweed type modulation towards the martensitic plate. **(d)** The growth of the martensitic plates from the nucleation sites.

transformation period.

A careful observation can lead to the interesting phase transformation event in some other grains, having tweed type contrast. Fig. 9 (b) shows some transient moment of the variation in tweed morphology. The white dotted box in Fig. 9(b), shows wavy or ripples type's nature of the composition fluctuation. Nucleation of martensite needle can be noticed from the wavy tweed zone as shown in Fig. 9(b) (Red marked arrows). Many literatures discussed on the lattice instability during martensitic transformation [34–36]. This pre-martensitic needle, emanating from the tweed type instability zone can be linked with those earlier findings [34–36]. Fig. 9(c) and (d) are the transient snapshot of different martensitic evolution stages, happening in different grain. In this transient period, tweed type zones are being converted into the martensite plates by regimented elastic lattice distortion. Fig. 9(c) and (d) also establish the fact that tweed type fluctuation actually acts as a precursor of pre-martensitic transformation [34–36, 42–43]. The disturbance in composition fluctuation and nucleation of martensitic plates can be related to the doping of copper in cobalt site. The changes of composition have a role in moderation of the martensitic transformation temperature (M_s = Martensitic Start, M_f = Martensitic Finish) and similar events can be noticed in this present study [40,41]. The transient spinodal fluctuation and related evolution of pre martensitic plates hint towards the compositional re-distribution of the alloy system. This composition re-distribution leads to the re-structuring of the shape of the interacting transformational free energies surfaces, involved in this quaternary alloy system. A detail thermodynamic calculation is currently being carried out to keep track on the modification of higher

order dimensional free energies involved in this multicomponent system.

The maturely grown alternating martensitic plates with average plate thickness of nearly 7 nm are shown in Fig. 10(a). A high-resolution phase contrast image of alternating martensite plates (yellow dotted box in Fig. 10(a)) is shown in Fig. 10(b). The spatial frequencies derived from the Fast Fourier Transform (FFT) method from the alternating martensitic variants marked as 1 and 2 are shown in Fig. 10(c) and (d) respectively. Appearance of different type of spatial frequencies, confirm the evolution of two different types of martensitic variants inside the B2 ordered Ni-Al rich grain. Streaking nature of the elongated diffraction frequencies along one direction can also be noticed from Fig. 10(c) and (d). This indicates the finite thickness at the martensitic variant interface. These self-accommodated variants minimize the transformation strain energy during nucleation of martensitic plates [44, 45]. The detailed TEM investigations hint towards the considerable extent of change in the evolved Ni-Al PIMA active grain of Alloy 2 in comparison to the undoped Co-Ni-Al alloy (Alloy 1). These changes can be directly linked to the retrogression of PIMA properties for this Alloy 2 as compared to undoped Alloy 1 [22–25].

Finally, we looked at the evolution of the microstructure of Alloy 4 in finer details. Fig. 11(a) shows the representative TEM bright field image of the Alloy 4. There is no such embedded grain type diffraction contrast is observed for this alloy. A selected area diffraction pattern taken along 111type of zone can be indexed as L1$_2$ ordered structure [46–48]. The white dotted box of Fig. 11(a) is the region from where the diffraction pattern is taken and shown in Fig. 11(b). This information indicates the
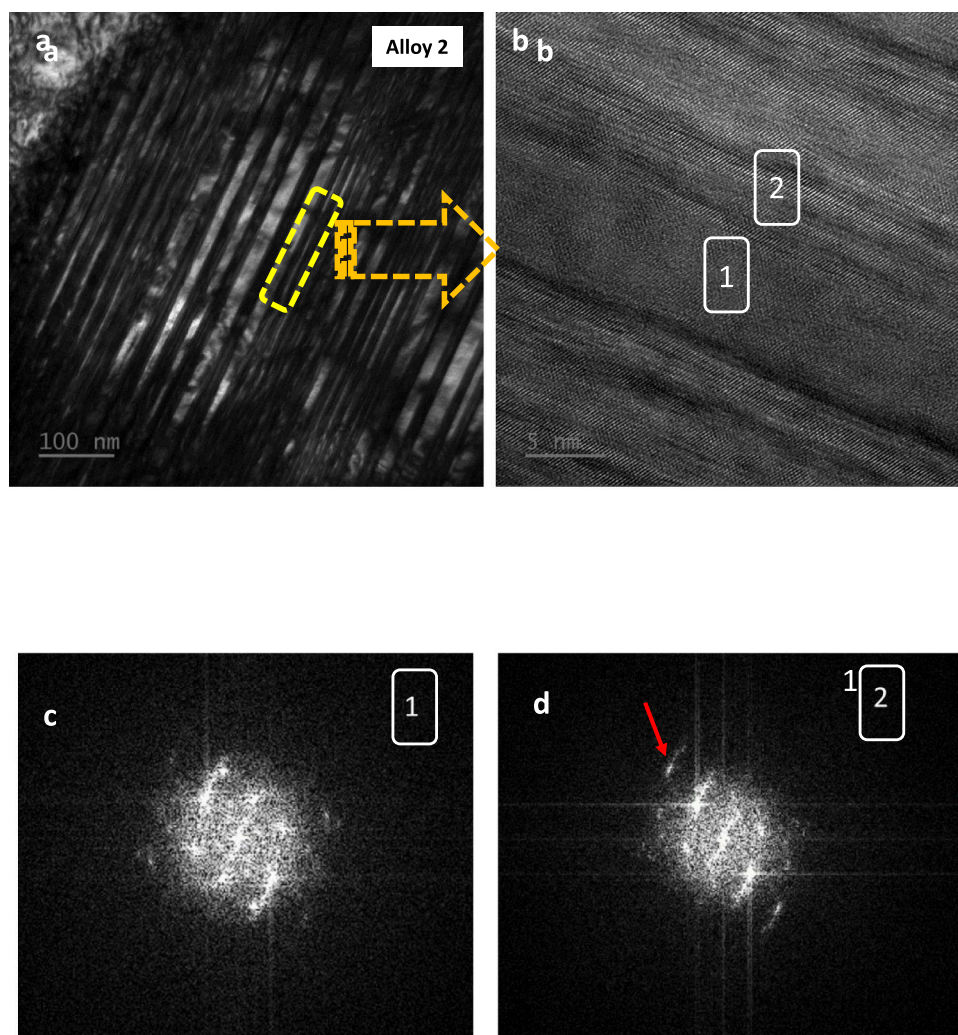
Fig. 10. (a) Bright field image showing the alternating martensitic plates. (b) Phase contrast high resolution micrograph of the martensitic plates. (c) and (d) Corresponding FFT diagram taken from location 1 and 2 of the (b).

evolution of the FCC based ordered solid solution in the microstructure instead of B2 order grain. This diffraction information can also be directly correlated with the XRD based comparative structural analysis as shown in Fig. 2(e). The comparative XRD study shows the evolution of FCC based signature peak for the case of Alloy 4, whereas, Alloy 2 has no such peaks in the entire Bragg angle scanning range. Some closer observation shows that, a few areas show some variation in atomic contrast as shown in the STEM-HAADF image in Fig. 11 (c). These are plausibly some unconverted Ni-Al rich B2 ordered grains with low volume fractions and their traces has also been captured during comparative XRD investigation (Fig. 2(e)). An EELS based spectral mapping as shown in Fig. 11(d-g) establishes the fact of equal partitioning of the elements and confirms the formation of solid solution. Few areas with darker contrast with rich in aluminium and devoid of nickel and copper (Fig. 11(c) and (g)) can be the trace of unconverted Ni-Al B2 ordered grains. It can be presumed that the substitution of aluminium by copper have an influence to disturb the ratio of Ni and Al inside the grains. The loss of aluminium has pushed the Ni-Al composition ratio towards the Ni_3Al or A_3B type of $L1_2$ ordered structure in the entire alloy system and thus can be tracked through the diffraction studies (Fig. 11(b)). The vanishing PIMA active B2 ordered Ni-Al grains can be directly associated with the ceasing of deflection for the case of Alloy 4. The entire microstructural, EBSD and XRD investigation place this analogy in a stronger foundation that B2 ordered Ni-Al rich grains are the key

effector for PIMA properties.

This special photo induced actuation can be presumed to be linked with plasmonic resonance on the alloy surface [49–52]. In this context, it intrigued us to investigate the role of plasmonic resonance pattern and behaviour of the studied alloys. STEM based EELS technique allow us to excite the low loss plasmonic spectrum from the targeted microstructural features of the developed alloys. This technique can access the information about the probability of excited plasmonic mode across the energy spread at each pixel position by scanning the fine electron beam probe [53–57]. The spectral intensity (SI) generated during raster scanning of the probe provides the plasmonic behaviour with some loss of spatial resolution. A combined low loss EELS spectrum in the plasmon region for the studied alloys are shown in figure12 (a) along with the reference zero loss peak (ZLP). The low loss spectrum of Alloy 2 with the existence of PIMA active B2 ordered Ni-Al rich grain and the matrix channel are shown separately (Red and Green spectrum of Fig. 12 (a)). It can be noticed qualitatively that similar nature of the plasmonic resonance can be observed from both the alloys. A deconvolution method of extracting the overlapping plasmon modes was only successful with the Alloy 2 sample. The deconvoluted modes from the PIMA active B2 ordered grains are shown in Fig. 12(b). Two prominent modes with loss energy of 19.0 eV and 24.3 eV are plotted in the red and green colour. A tail peak at around 37.5 eV is presented in blue legend of Fig. 12(b). The plasmonic behaviour from the Alloy 4 sample, only shows a main peak at
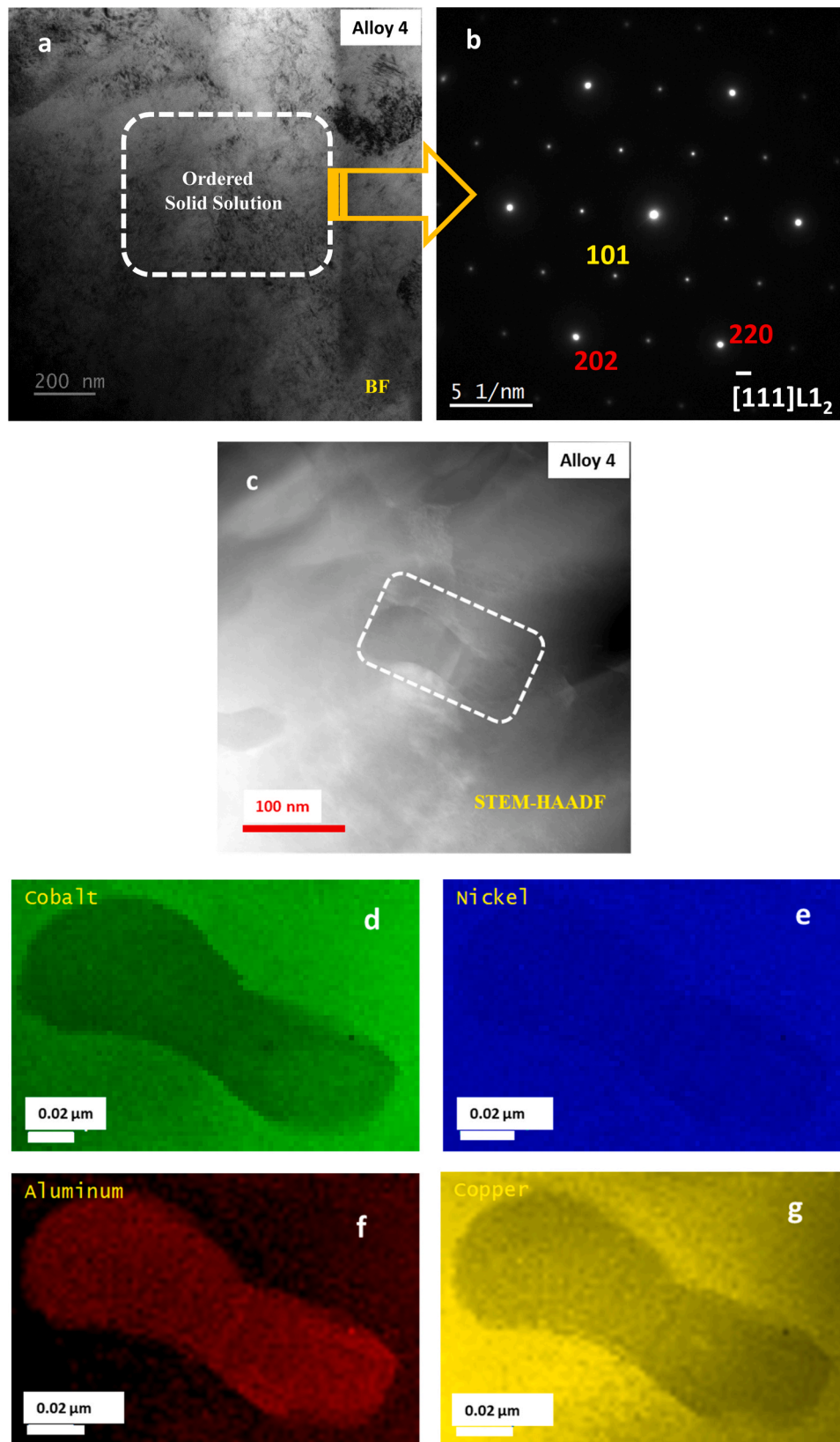
Fig. 11. (a) A representative Bright Field micrograph showing the homogeneous $L1_2$ ordered solid solution structure. (b) A 111 zone axis diffraction pattern. (c) An STEM-HAADF micrograph showing the vanishing of B2 ordered grain for the Alloy 4. (d-g) Spatial Elemental distribution maps derived from EELS spectrum showing qualitatively equal partition of all the elements.
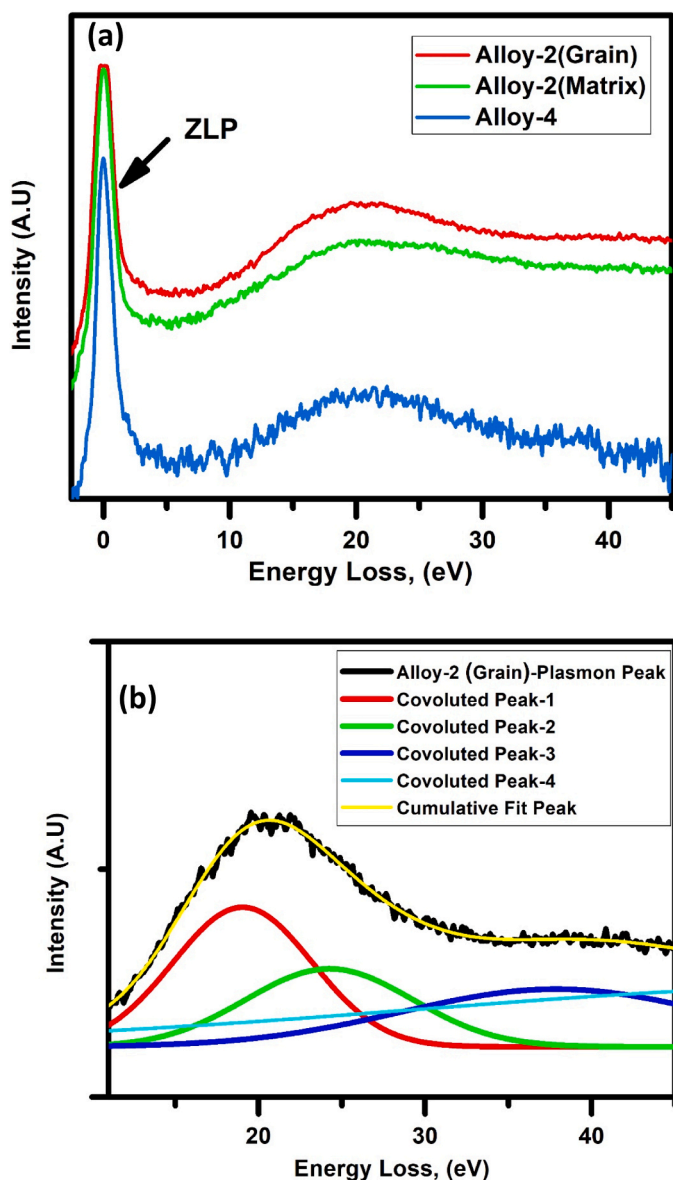
Fig. 12. (a) A combined low loss EELS spectra in the plasmon region for the studied alloys. (b) Deconvoluted Plasmon Spectra from the PIMA active B2 ordered grain of the Alloy 2 showing the exitance of overlapped plasmonic signature in the low loss region.

20.3 eV. The plasmonic energy response modes maps are generated by plotting the spectral intensity and selecting the energy loss window. The plasmonic modes maps for three different energy loss windows as derived from the deconvoluted data for Alloy 2 and similar energy windows for Alloy 4 are shown in Fig. 13(a-c) and (d-f) respectively. The signal acquisition position during mapping is shown in Fig. 13(h) and (i) from the earlier described STEM-HAADF images for two alloys. Fig. 13 (a) and (b) show the distinction in the signal intensity at 9–16 eV and 15–27 eV energy window between the matrix channel and B2 ordered Ni-Al grains for Alloy 2. The interfacial region between matrix channel and grain has also demonstrated the diffused nature of the intensity variation in these energy windows. An intensity range bar is also included in the Fig. 13. This intensity variation can be connected with the compositional and structural differences of the phases (grain and matrix). This difference has also similar impact on the plasmonic response between matrix and B2 ordered grains and this has been captured through this EELS based spectroscopic analysis. At 30–42 eV

energy loss window, this variation persists with gradation in intensity as shown in Fig. 13(c). It is interesting to observe that for the case of Alloy 4, the spectral intensity variation is absent for similar energy windows. This confirms the homogeneous formation of single ordered solid solution region with identical structure and composition in the entire microstructure as determined from the diffraction data (Fig. 11(b)). A one-dimensional line spectral intensity variation profile for the two studied alloys is also shown in 13(g) (along the white and black dotted lines in Fig. 13(b) and (e)). This one-dimensional variation also complements the observation derived from the plasmonic mode maps. This energy loss spectral analysis exercise conveys the importance of the presence of B2 ordered Ni-Al grains for the observed photo induced actuation for the case of Alloy 2. A single homogeneous FCC based ordered solid solution structure is not capable of offering the needed laser-based actuation for the Alloy 4.

3.3. Scanning probe microscopy studies

3.3.1. AFM analysis and constitutive properties determination

The Young's Modulus (E) of the alloy samples was measured by employing the contact mode point spectroscopy method [27–30] in AFM. As mentioned earlier, analysis of the Force-Distance curve obtained from this experimental technique was used to measure the elastic modulus of the sample. The Hertzian model modified by Snedon was used to determine the required elastic modulus [27–30]. From this model the relationship between the applied force (F) and the indentation depth (δ) can be determined through the Young's Modulus (E) and Poisson's Ratio (ν) of the studied samples. Assuming the cantilever beam of the AFM apparatus to be linearly elastic having a specified spring constant (k), Hook's Law can be applied here to find the relation between applied loading force and cantilever deflection (D). The equation used for this purpose is as follows.

$$kD = \frac{2E\tan(\alpha)}{\pi(1-\nu^2)}\delta^2 \tag{1}$$

In this equation, (α) is the half opening angle of the probe tip. The constant values used for solving this equation for determination of Young's Modulus (E) of the samples are provided in the experimental section. The Force-Distance curves of alloy 2 is plotted in Fig. 14 (a). The Young's Modulus of the alloy 2 was determined using Eq. (1). It is turns out to be 20.75 GPa approximately. The mechanical data are not included for the case of alloy 4 as this does not demonstrate any actuation. The evaluated experimental value was directly used for the description of the FEM model.

3.3.2. Magnetic force microscopy

In our earlier studies, we have noticed some interesting observation regarding the magnetic properties of studied alloys [22]. The sudden jump of the saturation magnetization was observed for alloy 4 even after the conservation of participating magnetic atom that is Co and Ni. The replacement of magnetic Co with diamagnetic Cu in the crystal lattice and a routine retrogression of diluted magnetic properties was quite a regular trend for alloy 2 [22]. In this present study, we have revisited the observation from a pictorial insight through MFM scanning for the studied alloys. The MFM generated multi domains maps and associated AFM topographical information obtained from a dual mode retrace AFM/MFM scanning are shown in Fig. 14 (b-e) for alloy 2 and 4 respectively. The visibility of magnetic domains is generated by the interaction of the MFM probe tip with the localized magnetic stray field of the sample surface [58–60]. This interaction imparts a finite change of the probe's cantilever oscillation and thus phase shifts occur [58–60]. The strength of the magnetic interaction directly influences the phase shifts and recorded shift are the signature of the magnetic force of the present magnetic domains. The evolution of the ferromagnetic domains as seen for both the alloys (Fig. 14(c) and (e)) are consistent with the ferromagnetic nature. The observation also confirms the presence of
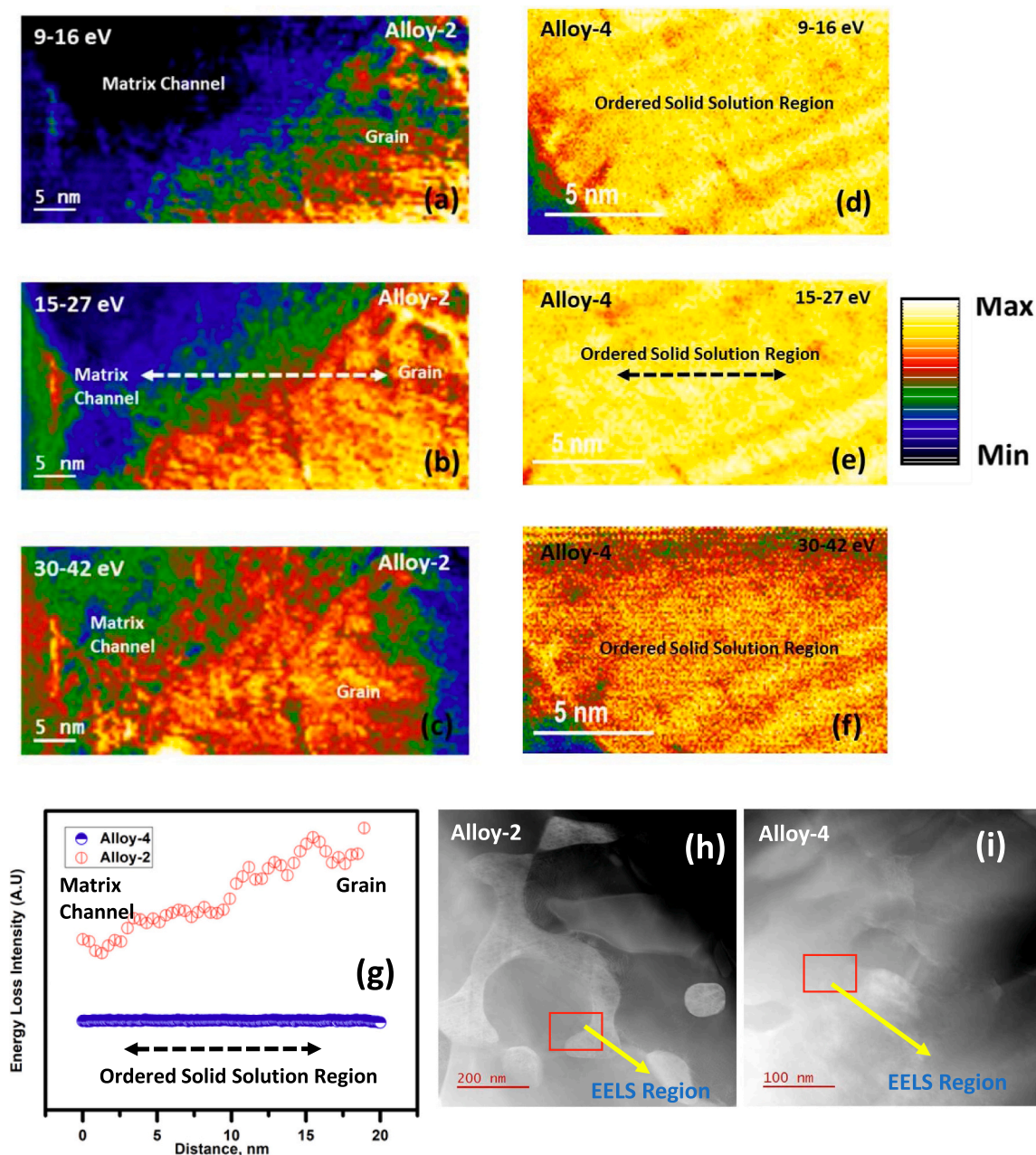
Fig. 13. (a-c) and (d-f) Plasmonic Energy Response mode maps generated at three loss energy domains for the Alloy 2 (covering the PIMA active grain and matrix channel together) and Alloy 4 (Ordered Solid Solution Region) over the SI. (g) 1 D Energy Loss spectral intensity variation for the two studied alloys. (h) and (i) Red rectangular box in the STEM-HAADF images of the studied alloys are the beam raster position used for the spectrum acquisition.

channel like interconnected domains from the out of plane magnetization component for the case of alloy 2 (Fig. 14(c)). If we consult the Fig. 5, the ferromagnetic Co rich L1$_2$ ordered matrix channel can be seen. In a similar note, a strong magnetic interaction and interconnected domain channels are also observed in the Fig. 14(c) (white dotted marker separating domain channel and grains in Fig. 14(c)) for alloy 2. In alloy 2, we have two distinct phases and their magnetic character are also different in nature. Whereas, in alloy 4, one can notice the evolution of a singular phase with L1$_2$ ordered structure as shown in Fig. 11. In this microstructure, homogeneous elemental partition with an ordered solid solution formation has been taken place (Fig. 11(d-e)). The signature of homogeneous microstructure and even distribution of magnetic element like Co and Ni are also reflected in the MFM scan for alloy 4. The leaching of magnetic element and singular phase formation offers

similar magnetic character for alloy 4. Fig. 14(e) (white dotted rectangular mark) also displays the distribution of circular magnetic domains in the phase shift map and complements the observed microstructural information. A normalized phase shift scan obtained from both the 2D MFM images for two alloys (from the white dotted mark areas for both the alloys in Fig. 14 (c) and (e)) is presented in Fig. 14(f). The line profile exhibits the gradient in magnetic behavior for alloy 2 from the channel to grain direction. On the contrary, alloy 4 demonstrates an alike pattern in the magnetic behavior with a presence of singular homogeneous solid solution phase. The leaching of ferromagnetic elements and a singular magnetic character in the microstructural volume may plausibly shoots up the magnetization values for alloy 4 as seen in the earlier quantitative studies [22,25]. It can also be inferred that only possessing ferromagnetic nature itself is not the sufficient condition for photo active
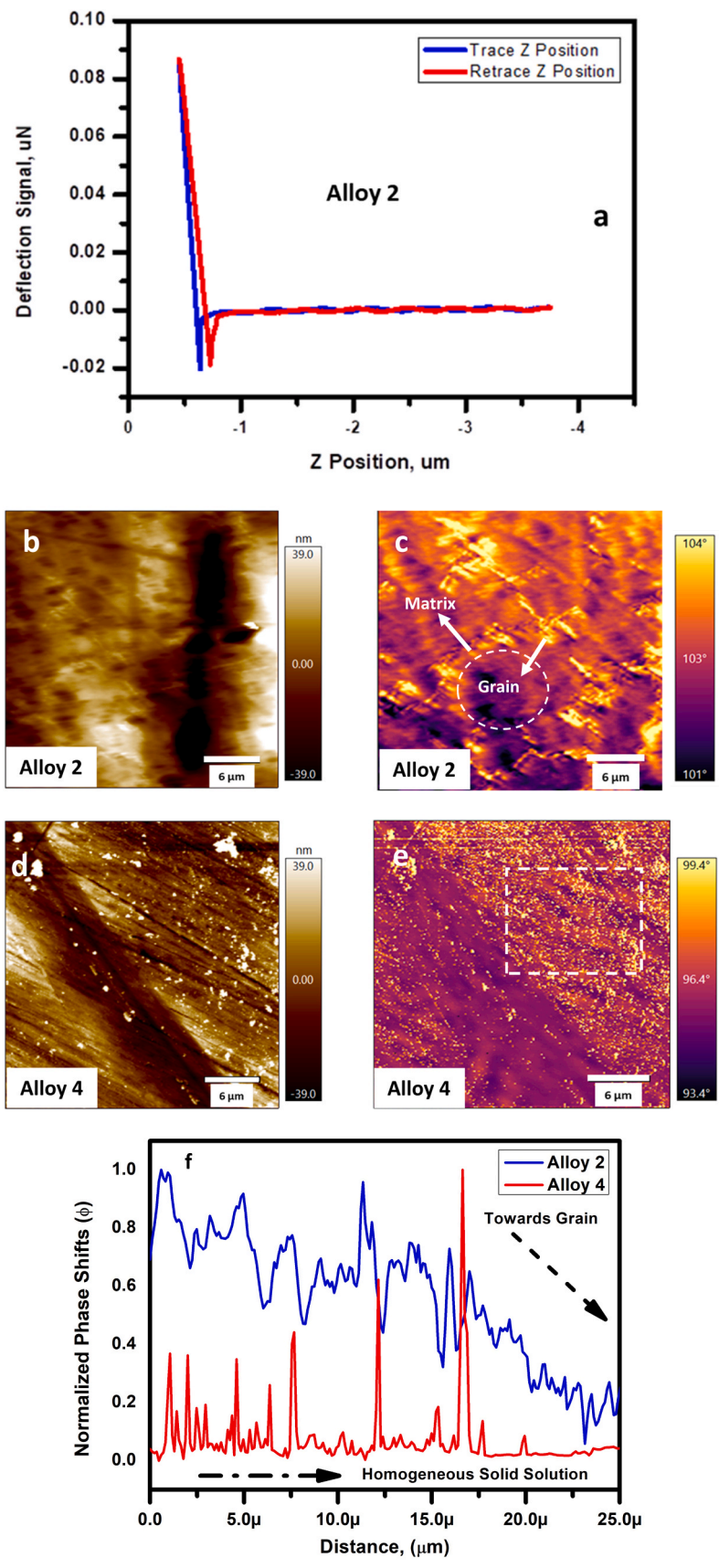
Fig. 14. (a) Force-Distance curve of Alloy 2. (b) and (c) AFM scanned topographical information of Alloy 2 and 4. (c) and (e) MFM based Phase Shifts retrace scan and the evolved domain structure information of Alloy 2 and Alloy 4. (f) A normalized phase shift profile displays the difference in magnetic behavior for two studied alloys.
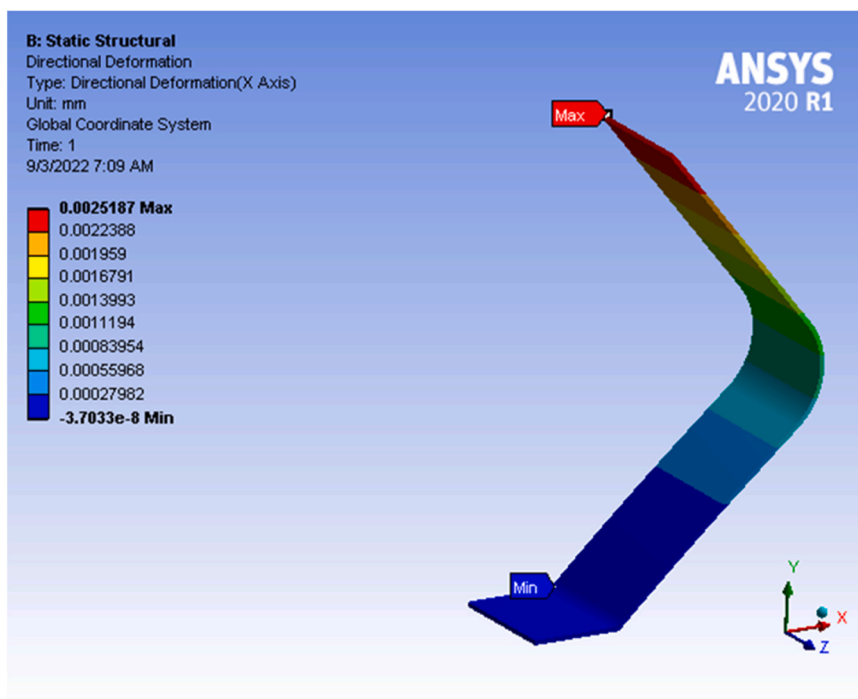
Fig. 15. Directional deflection of the free end of the Alloy 2 strip.

actuation. This current study and its related characterization, comprehensively indicates that the simultaneous existence of B2 type Ni-Al phase accompanied by ferromagnetic property are the necessary conditions for photo active actuation.

3.4. FEM analysis of the FSMA-PIMA active alloy strip

Deflection suffered by the FSMA alloy upon imposition of laser beam depends on the force experienced by that strip. The frequency of the incident light is a sensitive function of the deflection [22–25]. To probe the general interaction behavior of any PIMA active material with any laser beam, it is required to measure the force that is generated during laser incidence with a specific wave length. As there is no device to measure this tiny force, help of numerical simulation has been adopted for this force-deflection pattern recognition. An optimization method termed as Response Surface Methodology has been deployed to refine this simulated force values [26, 61–62]. Understanding the force distribution pattern may help in designing the real PIMA active engineering device and component. The intricate component of model set up, adopted boundary conditions and simulation methodology have been provided as supplementary information. The materials constitutive properties required for the FEM analysis are derived from the experimental results as well as from the AFM-Force-Distance data [22].

The ranges of assigned force values have been decided on the basis of experimental deflection values of the free end of the alloy strip (Table 2) [22]. Force values corresponding to the minimum and maximum values of directional deflections of the free end of the alloy strip are tabled in table S2 as supplementary information. These values have been determined in ANSYS by trial-and-error method. After determination of the maximum and minimum values of forces, a set of force values have been generated with a predefined interval after determination of the maximum and minimum values of forces.

Directional deflections of the free end of the alloy strip have been determined under the action of various forces between the maximum and minimum values as mentioned above using ANSYS. To perform this simulation, 'Large Deflection' parameter was kept on in the 'Simulation'

settings. Directional deflection of the free end of the alloy strip derived in ANSYS using a force value is shown in Fig15. The predicted output has been recorded as the evolved forces that the alloy strip might be experiencing corresponding to a particular value of directional deflection arising from the varied laser power and wavelength. The optimized forces in milli newton have been determined by putting the specific target values of deflections as per the experimental results in back process (Table 2) [22]. The determined micro forces which the alloy 2 strip might have experienced due to the imposition of laser beam of a particular wattage and color is presented in Fig. 16 (b). The laser Power v/s Free end deflection of the alloy 2 strip for three laser colors is also included in Fig. 16(a). The presented results show the deflecting capacity of the alloy strip in terms of force distribution. This information can be directly utilized for designing a real engineering device which can perform a customized work load in a tiny scale in an optically controlled remote operation situation. We are presently working on a prototype design of an optically controlled actuator from this alloy strip.

4. Conclusions

In this present study, microstructural influence on the Photo Induced Actuation properties of the Cu-doped Co-Ni-Al FSMA system has been evaluated in details. The microstructural length scale stability and generalized microstructural features required for PIMA properties has also been established. The role of the surface plasmonic effect for actuation has been investigated through STEM-EELS analysis. The magnetic domain nature for the alloy system has been probed thorough MFM technique. The necessary presence of PIMA active Ni-Al rich phase for actuation and its structural attributes have been explored for the optimized alloy. The invisible tiny force distribution pattern evolved during light matter interaction has been evaluated through FEM analysis. The FEM based model and its simulated results can be applied for real time PIMA oriented engineering application and device manufacturing.
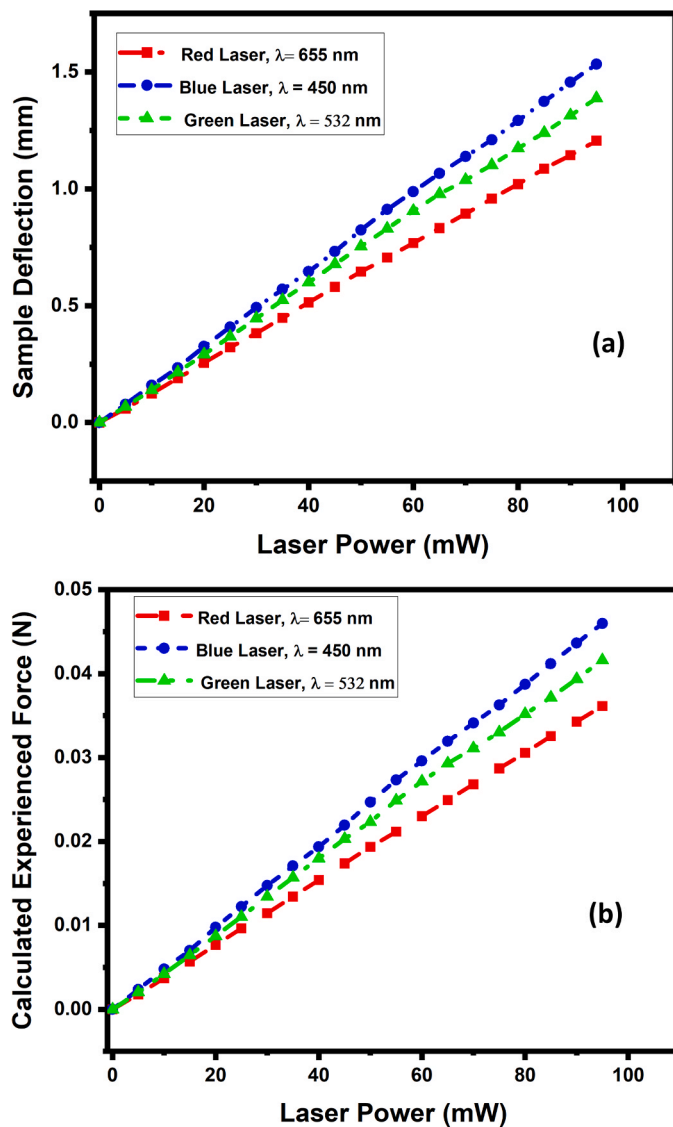
Fig. 16. (a) Laser Power v/s Free end deflection of the Alloy 2 strip for three laser colors. (b) Laser Power v/s Force experienced by the Alloy 2 strip for three laser colors.

CRediT authorship contribution statement

Abhishek Bagchi: Conceptualizing, Data analysis, Interpretation, Overall management. **Vidhyadhar Mishra:** Experiment, Data analysis. **Suman Sarkar:** Experiment, Data analysis. **Sandip Bysakh:** Microscopy, Sample curation. **K. Das Gupta:** Sample preparation. **T. Maity:** Sample preparation. **Amalendu Biswas:** FEM analysis. **Susenjit Sarkar:** FEM analysis. **P. K. Mukhopadhyay:** Optical experiment conceptualizing and overall project management. **Suman Sarkar:** Electron microscopy, MFM, EELS study, Conceptualizing, Data analysis, Overall project management.

Declaration of Competing Interest

The authors declare that they have no known competing financial interests or personal relationships that could have appeared to influence the work reported in this paper.

Data availability

Data will be made available on request.

Appendix A. Supporting information

Supplementary data associated with this article can be found in the online version at doi:10.1016/j.jallcom.2023.172262.

References

[1] Sangmo Koo, Advanced micro-actuator/robot fabrication using ultrafast laser direct writing and its remote control, Appl. Sci. 10 (2020) 8563, https://doi.org/10.3390/app10238563.
[2] P. Sente, H. Buyse, From smart sensors to smart actuators: application of digital encoders for position and speed measurements in numerical control systems, Measurement 15 (1995) 25–32.
[3] H.S. Tzou, C.-S. Chou, Nonlinear opto-electromechanics and photo deformation of optical actuators, Smart Mater. Struct. 5 (1996) 230–235.
[4] Seung Hui Han, Seok-In Lim, Ki-Hyun Ryu, Jahyeon Koo, Dong-Gue Kang, Kwang-Un Jeong, Seung-Yeol Jeon, Dae-Yoon Kim, Chiroptical 3D actuators for smart sensors, Adv. Funct. Mater. 33 (2023), 2210680, https://doi.org/10.1002/adfm.202210680.
[5] Z. Yanha, J. Terrien, L. Petit, H.A.L. Hajjar, O. Carton, S. Charvet, A. Zeinert, F. Lamarque, Optical Remote Control of an Electromagnetic Digital Actuator, MECATRONICS - REM 2016 June 15–17, 978–1-5090–1787-4/16/$31.00 ©2016 IEEE 2016.
[6] J. Bryzek, "Impact of MEMS technology on society", Sens. Actuators A 56 (1) (1996).
[7] J.W. Judy, Microelectromechanical systems (MEMS): fabrication, design and applications, Smart Mater. Struct. 10 (2001) 1115.
[8] A. Sozinov, N. Lanska, A. Soroka, W. Zou, "12% magnetic field-induced strain in Ni-Mn-Ga-based non-modulated martensite", Appl. Phys. Lett. 102 (2013), 021902.
[9] A. Sozinov, A.A. Likhachev, K. Ullakko, "Magnetic and magneto-mechanical properties of Ni-Mn-Ga alloys with easy axis and easy plane of magnetization", Proc. SPIE 4333 (2001) 189.
[10] C.P. Henry, P.G. Tello, D. Bono, J. Hong, R. Wagner, J. Dai, S.M. Allen, R. C. O'Handley, "Frequency response of single-crystal Ni-Mn-Ga FSMAs", Proc. SPIE 207 (2003).
[11] C. Naresh, P.S.C. Bose, C.S.P. Rao, Shape memory alloys: a state of art review, IOP Conf. Ser.: Mater. Sci. Eng. 149 (2016), 012054, https://doi.org/10.1088/1757-899X/149/1/012054.
[12] Jaronie Mohd Jani, Martin Leary, Aleksandar Subic, Mark A. Gibson, A review of shape memory alloy research, applications and opportunities, Mater. Des. (1980-2015) Volume 56 (2014) 1078–1113.
[13] Peng Hua, Minglu Xia, Yusuke Onuki, Qingping Sun, Nanocomposite NiTi shape memory alloy with high strength and fatigue resistance, Nat. Nanotechnol. | VOL 16 (2021) 409–413, https://doi.org/10.1038/s41565-020-00837-5.
[14] Lin Yu, Keyu Chen, Yuanling Zhang, Jie Liu, Lei Yang, Yusheng Shi, Microstructures and mechanical properties of NiTi shape memory alloys fabricated by wire arc additive manufacturing, J. Alloy. Compd. Volume 892 (2022), 162193, https://doi.org/10.1016/j.jallcom.2021.162193.
[15] L. Pan-Pan, W. Jing-Min, J. Cheng-Bao, Martensitic transformation in Cu-doped NiMnGa magnetic shape memory alloys", Chin. Phys. B 20 (2011), 028104.
[16] J. Ju, H. Liu, L. Shuai, Z. Liu, Y. Kang, C. Yan, H. Li, "Martensite transformation and mechanical properties of polycrystalline Co-Ni-Al alloys with Gd doping", Metals 8 (2018) 848.
[17] C. Tan, Z. Tai, K. Zhang, X. Tian, W. Cai, Simultaneous enhancement of magnetic and mechanical properties in Ni-Mn-Sn alloy by Fe doping", Sci. Rep. 7 (2017) 43387.
[18] Atefeh Sadeghzadeh, Estibalitz Asua, Jorge Feuchtwanger, Victor Etxebarria, Alfredo García-Arribas, Ferromagnetic shape memory alloy actuator enabled for nanometric position control using hysteresis compensation, Sens. Actuators A: Phys. Volume 182 (2012) 122–129.
[19] M. Kohl, Y. Srinivasa Reddy, F. Khelfaoui, B. Krevet, A. Backen, S. Fähler, T. Eichhorn, G. Jakob, A. Mecklenburg, Recent progress in FSMA microactuator developments, Mater. Sci. Forum Vol. 635 (2010) 145–154.
[20] Racil Jeya Geetha, R.Senthur Pandi, S. Seenithurai, S.Vinodh Kumar, M. Muthuraman, J.Thampi Thanka Kumaran, M. Mahendran, Vibration damping in Ni-Mn-Ga/PU polymer composites, Int. J. Compos. Mater. 1 (1) (2011) 1–6, https://doi.org/10.5923/j.cmaterials.20110101.01.
[21] Z. Hu, B. Rajini Kanth, R. Tamang, B. Varghese, C.H. Sow, P.K. Mukhopadhyay, Visible microactuation of a ferromagnetic shape memory alloy by focused laser beam, Smart Mater. Struct. 21 (2012), 032003.
[22] Abhishek Bagchi, Suman Sarkar, Sandip Bysakh, Chandra Sekhar Tiwary, Md. Sarowar Hossain, Susenjit Sarkar, P.K. Mukhopadhyay, Microstructural evolution and its outcome on the photo induced micro actuation effect and mechanical properties of copper doped Co-Ni-Al FSMA, J. Alloy. Compd. Vol.846 (2020), 156432.

[23] Abhishek Bagchi, Suman Sarkar, Sandip Bysakh, Susenjit Sarkar, P. K. Mukhopadhyay, Studies on effect of temperature on the Photo Induced Micro-Actuation effect of a Co-based FSMA system, J. Shape Mem. Superelasticity (2020), https://doi.org/10.1007/s40830-020-00270-6.

[24] A. Bagchi, S. Sarkar, P.K. Mukhopadhyay, Investigations on colour dependent photo induced microactuation effect of FSMA and proposing suitable mechanisms to control the effect, Indian J. Phys. 92 (2018) 883.

[25] A. Bagchi, S. Sarkar, S. Bysakh, S. Sarkar, P.K. Mukhopadhyay, Possible mechanisms for degradation of photo induced micro actuation effect in a ferromagnetic shape memory alloy at high temperatures, J. Appl. Phys. 125 (2019), 144505.

[26] Abhishek Bagchi, Amalendu Biswas, Gurdeep Singh, Susenjit Sarkar, P. K. Mukhopadhyay, Finite element analysis of a FSMA microgripper for determination of force experienced by it due to photo induced micro actuation effect, J. Micro-Bio Robot. (2022), https://doi.org/10.1007/s12213-022-00147-0.

[27] J. Kámán, Young's modulus and energy dissipation determination methods by AFM, with particular reference to a chalcogenide thin film, Period. Polytech. Electr. Eng. Comput. Sci. 59 (1) (2015) 18–25, https://doi.org/10.3311/PPee.7865.

[28] H. Hertz, Ueber die Berührung fester elastischer Körper, J. für die reine und Angew. Math. (1882) 156.

[29] H.J. Butt, B. Cappella, M. Kappl, Force measurements with the atomic force microscope: Technique, interpretation and applications, Surf. Sci. Rep. 59 (1) (2005).

[30] J. Domke, M. Radmacher, Measuring the elastic properties of thin polymer films with the AFM, Langmuir 14 (1998) 3320.

[31] A.A. Salem, M.G. Glavicic, S.L. Semiatin, A coupled EBSD/EDS method to determine the primary- and secondary-alpha textures in titanium alloys with duplex microstructures, Mater. Sci. Eng.: A Volume 494 (Issues 1–2) (2008) 350–359.

[32] A.E. Davis, X. Zeng, R. Thomas, J.R. Kennedy, J. Donoghue, A. Gholinia, P. B. Prangnell, J.Quinta Da Fonseca, Optimising large-area crystal orientation mapping of nanoscale β phase in α + β titanium alloys using EBSD, Mater. Charact. 194 (2022), 112371, https://doi.org/10.1016/j.matchar.2022.112371.

[33] Angus J. Wilkinson, T.Ben Britton, Strains, planes, and EBSD in materials science, Mater. Today 15 (9) (2012) 366–376, https://doi.org/10.1016/S1369-7021(12)70163-3.

[34] Le Zhou, Matthew M. Schneider, Anit Giri, Kyu Cho, Yongho Sohn, Microstructural and crystallographic characteristics of modulated martensite, non-modulated martensite, and pre-martensitic tweed austenite in Ni-Mn-Ga alloys, Acta Mater. 134 (2017) 93–103, https://doi.org/10.1016/j.actamat.2017.05.050.

[35] R.V.S. PRASAD, M. SRINIVAS, M. MANIVEL RAJA, G. PHANIKUMAR, Microstructure and Magnetic Properties of Ni2(Mn,Fe)Ga Heusler Alloys Rapidly Solidified by Melt Spinning, Metall. Mater. Trans. A 45A (2014) 2161, https://doi.org/10.1007/s11661-013-2124-x.

[36] R. OSHIMA, M. SUGIYAMA, E.E. FUJITA, Tweed structures associated with Fcc-Fct transformations in Fe-Pd alloys, Metall. Trans. A 19A (1988) 803.

[37] Jingjing Yang, Chunyang Zhao, Hailong Liang, Zemin Wang, Chenyu Su, Spinodal decomposition and martensitic transformation of the high manganese Mn–xCu alloys fabricated by additive manufacturing, Appl. Mater. Today 25 (2021), 101170, https://doi.org/10.1016/j.apmt.2021.101170.

[38] B.J. Park, H.J. Chang, D.H. Kim, W.T. Kim, K. Chattopadhyay, T.A. Abinandanan, S. Bhattacharyya, Phase separating bulk metallic glass: a hierarchical composite, PRL 96 (2006), 245503.

[39] Tianlong Zhang, Dong Wang, Yunzhi Wang, Novel transformation pathway and heterogeneous precipitate microstructure in Ti-alloys, Acta Mater. 196 (2020) 409–417.

[40] W. Maziarz, J. Dutkiewicz, R. Santamarta, E. Cesari, Microstructure changes in two phase β + γ Co-Ni-Al ferromagnetic shape memory alloys in relation to Al/Co ratio", Eur. Phys. J. Spec. Top. 158 (2008) 137.

[41] J. Ju, L. Yang, S. Hao, Q. Mao, S. Lou, H. Liu, Microstructure, martensite transition and mechanical properties investigations of polycrystalline Co-Ni-Al alloys with Er doping, J. Mater. Eng. Perform. 26 (2017) 1062.

[42] Yongmei M. Jin, Yu.U. Wang, Yang Ren, Theory and experimental evidence of phonon domains and their roles in pre-martensitic phenomena, npj Comput. Mater. 1 (2015), 15002, https://doi.org/10.1038/npjcompumats.2015.2.

[43] Y. MURAKAM I, H. SH IBUYA, D. SH INDO, Precursor effects of martensitic transformations in Ti-based alloys studied by electron microscopy with energy filtering, J. Microsc. Vol. 203 (Pt 1) (2001) 22–33.

[44] Jingyi Cao, Jianfeng Jin, Shaojie Li, Mingtao Wang, Shuai Tang, Qing Peng, Yaping Zong, Effect of microstructure on the onset strain and rate per strain of deformation-induced martensite transformation in Q&P steel by modeling. Materials 15 (3) (2022) 952, https://doi.org/10.3390/ma15030952.

[45] Yildirim Aydogdu, Ayse Aydogdu, Osman Adiguzel, Self-accommodating martensite plate variants in shape memory CuAlNi alloys, J. Mater. Process. Technol. 123 (2002) 498–500.

[46] Suman Sarkar, Shyam Kanta Sinha, Dhanalakshmi Palaniswamy, Chandan Srivastava, Kamanio Chattopadhyay, Evolution of $L1_2$ ordered precipitates in Cu–Fe–Si alloy system and its influence on potential strength–conductivity properties. Metallogr. Microstruct. Anal. 12 (2023) 134–149, https://doi.org/10.1007/s13632-023-00938-2.

[47] S. Sarkar, C. Srivastava, K. Chattopadhyay, "Development of a new class of high strength copper alloy using immiscibility route in Cu-Fe-Si system: Evolution of hierarchical multi-scale microstructure", Mater. Sci. Eng. A 723 (2018) 38.

[48] H.Y. Wang, K. Wang, Z.H. Liu, Y.G. Wang, G.H. Wu, X.F. Duan, "TEM characterization of twinning in Co39Ni33Al28 alloy", Mater. Trans. 48 (8) (2007) 2139.

[49] Min-Soo Kim, Hye-Sung Lee, Younggyun Cho, Jae Kyung Heo, Ying-Jun Quan, Seung Woo Lee, Heui Jae Pahk, Sung-Hoon Ahn, Surface Nanopatterned Shape Memory Alloy (SMA)-based photosensitive artificial muscle, Adv. Opt. Mater. 10 (2022) 2102024, https://doi.org/10.1002/adom.202102024.

[50] Gautham Kumar, Ganesh D. Sharma, Fang-Chung Chen, Localized surface plasmon resonance of Au–Cu alloy nanoparticles enhances the performance of polymer photovoltaic devices for outdoor and indoor applications, Opt. Mater. Express Vol. 11 (No. 4 / 1) (2021) (April).

[51] Qilin Duan, Yineng Liu, Shanshan Chang, Huanyang Chen, Jin-hui Chen, Surface plasmonic sensors: sensing mechanism and recent applications, Sensors 21 (16) (2021) 5262, https://doi.org/10.3390/s21165262.

[52] Reza Mokhtarpour, Habib Badri Ghavifekr, Design and optimization of surface plasmonic sensor with tunable optical actuation angle based on microsystem technology for microfluidic application, Plasmonics volume 17 (2022) 2131–2140.

[53] Yueying Wu, Guoliang Li, Jon P. Camden, Probing nanoparticle plasmons with electron energy loss spectroscopy, Chem. Rev. 118 (6) (2018) 2994–3031, https://doi.org/10.1021/acs.chemrev.7b00354.

[54] Magnus Garbrecht, Lars Hultman, Mohammed H. Fawey, Timothy D. Sands, Bivas Saha, Tailoring of surface plasmon resonances in TiN/ $(Al_{0.72}Sc_{0.28})N$ multilayers by dielectric layer thickness variation, J. Mater. Sci. 53 (2018) 4001–4009.

[55] Ina Schubert, Maria Eugenia Toimil-Molares, Plasmonic Modes in Au and AuAg Nanowires and Nanowire Dimers Studied by Electron Energy Loss Spectroscopy, IntechOpen,, 2018, https://doi.org/10.5772/intechopen.79189.

[56] Robyn Collette 1, David A. Garfinkel 1, Zhongwei Hu 2, David J. Masiello 2, Philip D. Rack, Near field excited state imaging via stimulated electron energy gain spectroscopy of localized surface plasmon resonances in plasmonic nanorod antennas, Sci. Rep. 10 (1) (2020 27), 12537, https://doi.org/10.1038/s41598-020-69066-z. PMID: 32719406; PMCID: PMC7385139.

[57] Collette, Robyn, "Exploration of binary metallic systems for plasmonic applications and stimulated electron energy gain spectroscopy of plasmonic nanostructures." PhD diss., University of Tennessee, 2020. https://trace.tennessee.edu/utk_graddiss/6794.

[58] O. Öztürk, M. Fidan, S. Mändl, MFM imaging of expanded austenite formed on 304 SS and CoCrMo alloys, Surf. Coat. Technol. 256 (2014) 15–22.

[59] B.R.A. Neves, M.S. Andrade, Identification of two patterns in magnetic force microscopy of shape memory alloys, Appl. Phys. Lett. VOLUME 74 (NUMBER 14) (1999).

[60] Krasimir Aleksandrov, Mathias C. Galetz, Gerald Schmidt, Francesco Depentori, Michael Schütze, Iulian Teliban, Eckhard Quandt, Protective high temperature coatings with intrinsic depletion sensor, Surf. Coat. Technol. 245 (2014) 117–124.

[61] Jin Xiangjie, Zhang Cai, Wang Chong, Response surface optimization of machine tool column based on ansys workbench, ACADEMIC J. Manuf. Eng. VOL.18 (ISSUE 2) (2020).

[62] S.C. Huang, T.P. Dao, Design and computational optimization of a flexure-based XY positioning platform using FEA-based response surface methodology, Int. J. Precis. Eng. Manuf. 17 (2016) 1035–1048, https://doi.org/10.1007/s12541-016-0126-5.

[63] Tadeusz Stolarski, Yuji Nakasone, Shigeka Yoshimoto, Engineering Analysis with ANSYS Software, Butterworth-Heinemann,, 2018.